JGR Atmospheres

Key Points:
- Droplet size distribution patterns observed in warm cumuli reflect the roles of collision-coalescence, secondary activation, and mixing
- The intra-cloud distribution of droplet spectral dispersion varies with aerosol loading
- Emulating the observed shape-parameter improves bulk estimations of collision-coalescence in models

Correspondence to:

L. Hernández Pardo,
l.hernandezpardo@mpic.de

Observed and Simulated Variability of Droplet Spectral Dispersion in Convective Clouds Over the Amazon

Lianet Hernández Pardo[1,2] [ID], Luiz A. T. Machado[1,2] [ID], Hugh Morrison[3] [ID], Micael A. Cecchini[4] [ID], Meinrat O. Andreae[1,5,6] [ID], Christopher Pöhlker[1], Ulrich Pöschl[1], Daniel Rosenfeld[7] [ID], Eder P. Vendrasco[2], Christiane Voigt[8,9] [ID], Manfred Wendisch[10] [ID], and Mira L. Pöhlker[1] [ID]

[1]Multiphase Chemistry Department, Max Planck Institute for Chemistry, Mainz, Germany, [2]Centro de Previsão de Tempo e Estudos Climáticos, Instituto Nacional de Pesquisas Espaciais, Cachoeira Paulista, Brazil, [3]Mesoscale and Microscale Meteorology Laboratory, National Center for Atmospheric Research, Boulder, CO, USA, [4]Institute of Physics, University of Sao Paulo, São Paulo, Brazil, [5]Scripps Institution of Oceanography, University of California San Diego, La Jolla, CA, USA, [6]Department of Geology and Geophysics, King Saud University, Riyadh, Saudi Arabia, [7]Institute of Earth Sciences, The Hebrew University of Jerusalem, Jerusalem, Israel, [8]Institut für Physik der Atmosphäre, Deutsches Zentrum für Luft und Raumfahrt, Wessling, Germany, [9]Institut für Physik der Atmosphäre, Johannes Gutenberg-Universität Mainz, Mainz, Germany, [10]Leipziger Institut für Meteorologie, Universität Leipzig, Leipzig, Germany

Abstract In this study, the variability of the spectral dispersion of droplet size distributions (DSDs) in convective clouds is investigated. Analyses are based on aircraft measurements of growing cumuli near the Amazon basin, and on numerical simulations of an idealized ice-free cumulus. In cleaner clouds, the relative dispersion ϵ, defined as the ratio of the standard deviation to the mean value of the droplet diameter, is negatively correlated with the ratio of the cloud water content (q_c) to the adiabatic liquid water content (q_a), while no strong correlation between ϵ and q_c/q_a is seen in polluted clouds. Bin microphysics numerical simulations suggest that these contrasting behaviors are associated with the effect of collision-coalescence in cleaner clouds, and secondary droplet activation in polluted clouds, in addition to the turbulent mixing of parcels that experienced different paths within the cloud. Collision-coalescence simultaneously broadens the DSDs and decreases q_c, explaining the inverse relationship between ϵ and q_c/q_a in cleaner clouds. Secondary droplet activation broadens the DSDs but has little direct impact on q_c. The combination of a rather modest DSD broadening due to weak collision-coalescence with enhanced droplet activation in both diluted and highly undiluted cloud regions may contribute to maintain a relatively uniform ϵ within polluted clouds. These findings can be useful for parameterizing the shape parameter (μ) of gamma DSDs in bulk microphysics cloud-resolving models. It is shown that emulating the observed $\mu - q_c/q_a$ relationship improves the estimation of the collision-coalescence rate in bulk microphysics simulations compared to the bin simulations.

1. Introduction

The realism of cloud microphysics parameterizations in weather and climate models has been improved over the last decades, with current schemes covering a wide spectrum of complexities (e.g., see reviews of Khain et al., 2015; Morrison et al., 2020). Bin and Lagrangian microphysics approaches are considered to be more accurate and flexible (e.g., Berry & Reinhardt, 1974; Enukashvily, 1980; Grabowski et al., 2018; Seifert et al., 2019; Shima et al., 2009; Tzivion et al., 1987), but their computational cost is usually too high for operational applications or large scale simulations. In such cases, bulk schemes (e.g., Ferrier, 1994; Lin et al., 1983; Morrison et al., 2009; Thompson et al., 2008) are employed. Instead of explicitly predicting the evolution of hydrometeors size distributions, bulk microphysics parameterizations compute conversion rates among several hydrometeor categories in terms of integral properties of their size distributions (typically, mass and number). Consequently, hydrometeors size distributions are usually assumed to follow predefined functional relationships, such as the gamma function:

$$N(D) = N_0 D^\mu e^{-\Lambda D} \tag{1}$$

where N_0, μ and Λ are the intercept, shape and slope parameters, respectively, and $N(D)$ is the number of droplets in a diameter interval $D + dD$ and in a unit volume of air. The assumption of a predefined function

for hydrometeor size distributions constitutes an intrinsic limitation of most bulk microphysics parameterizations. For instance, although droplet size distributions (DSDs) averaged over large regions and different clouds can be relatively well represented by the gamma function, local DSDs can present specific features, such as bi-modalities, that significantly deviate from the average gamma-like shape (Khain et al., 2015). Moreover, bulk schemes must predict at least three moments to evolve the three gamma size distribution parameters independently, and schemes predicting fewer moments must introduce additional closure assumptions. In the case of double-moment schemes that assume gamma size distributions, empirical methods are generally employed in order to determine the μ parameter.

If the DSD follows a gamma function, $\mu = \epsilon^{-2} - 1$, where ϵ is the relative dispersion (defined as the ratio of the standard deviation σ to the mean value D_m of the droplet diameter). μ is also related to the parameter $\beta = \left[\dfrac{(\mu + 3)^2}{(\mu + 2)(\mu + 1)} \right]^{1/3}$, which represents the ratio of the effective radius to the volume mean radius of cloud droplets (Liu & Daum, 2002; Peng & Lohmann, 2003).

Many mechanisms may explain the DSD broadening observed in real clouds, compared to the spectral width predicted by condensational growth in an ascending, adiabatic, non-turbulent parcel. Among these mechanisms are the effect of solute and curvature on the condensation/evaporation occurring in vertically oscillating parcels (Jensen & Nugent, 2017; Korolev, 1995; Yang et al., 2018; Yin et al., 2000); the impact of radiative cooling at cloud top (Hartman & Harrington, 2005a, 2005b; Lebo et al., 2008); turbulence enhancement of collisions (Ayala, Rosa, Wang, & Grabowski, 2008; Ayala, Rosa, & Wang, 2008; Chen, Yau, & Bartello, 2018; Dávila & Hunt, 2001; Devenish et al., 2012; Franklin et al., 2005; Grabowski & Wang, 2013; J. Lu et al., 2010; Pinsky et al., 2006, 2007; L.-P. Wang et al., 2008); entrainment (Baker & Latham, 1979; Baker et al., 1980; Blyth, 1993; Brenguier & Grabowski, 1993; Cooper et al., 2013; Hoffmann et al., 2015; Latham & Reed, 1977; Tölle & Krueger, 2014); and the mixing of droplets that have experienced different condensational growth histories in the clouds (Abade et al., 2018; Baker et al., 1984; Cooper, 1989; Dodson & Small Griswold, 2019; Grabowski & Abade, 2017; Lasher-Trapp et al., 2005). Such a diversity of factors determining the DSD shape makes the description of μ in single- or double-moment bulk schemes extremely difficult.

Several methods have been suggested for diagnosing μ in bulk schemes. In previous studies, μ (or ϵ, or β) was commonly assumed to be correlated with the cloud droplet number concentration (N_c) or the aerosol number concentration (N_a), either positively (Grabowski, 1998) or negatively (Morrison & Grabowski, 2007; Peng & Lohmann, 2003; Rotstayn & Liu, 2003; Thompson et al., 2008), based on aircraft observations (Squires, 1958a; Squires, 1958b; MacCready & Takeuchi, 1968; G. Martin et al., 1994; Pawlowska et al., 2006). To account for factors that explain those two opposite correlations between μ (or ϵ, or β) and N_a found in observations, Liu et al. (2006) derived a diagnostic expression that considers the effect of the updraft speed (w), based on classical condensational growth theory under adiabatic conditions. Later, Liu et al. (2008) obtained an empirical relationship that describes the variations of DSD shape as a function of the mean droplet mass based on observations. The expression for μ developed by Khvorostyanov and Curry (1999, 2008) from analytical solutions of the kinetic equation of stochastic condensation attempts to reproduce the variability in DSD shape observed inside different clouds. It predicts both an increase and a decrease in μ with height depending on the balance among the effects of height above cloud base (h), dynamics (updraft strength and turbulence), and adiabaticity. However, among many simplifications, they assume that the variation of $N(D)$ with height does not depend on D, which might be a sufficient approximation for thin clouds only. Evaluating the expression of Khvorostyanov and Curry (1999) using observations is subject to large uncertainty related to estimating the eddy diffusivity coefficient, and its implementation in models requires accurate estimations of the subgrid vertical velocity.

In general, defining μ in terms of the model resolved quantities is uncertain, especially considering the high variability of observed μ values (Miles et al., 2000). In turn, these uncertainties impact the calculation of microphysical process rates and therefore the evolution of clouds in the simulations (e.g., Igel & van den Heever, 2017). For example, for a cumulus cloud simulated with bulk microphysics using a kinematic framework, Morrison and Grabowski (2007) obtained a $\sim 75\%$ increase in cloud water path when μ varied from ~ 4.95 to ~ 12.72, considering $N_c \sim 300 \text{ cm}^{-3}$.

Table 1

General Characteristics of the ACRIDICON-CHUVA Cloud Profiling Missions Referred in This Study: Aerosol Number Concentration (N_a), Cloud Condensation Nuclei Number Concentration (N_{CCN}) for Supersaturation S = 0.48 ± 0.033% and Cloud Base Altitude (z_{base})

Region	Flight	Name	N_a (cm^{-3})	N_{CCN} (cm^{-3})	z_{base} (m)
Atlantic coast	AC19	M1	465	119	550
Remote Amazon	AC09	RA1	821	372	1125
	AC18	RA2	744	408	1650
Arc of Deforestation	AC07	AD1	2498	1579	1850
	AC12	AD2	3057	2017	2140
	AC13	AD3	4093	2263	2135

Note. The names in the third column have the following meaning: M1 – Maritime 1; RA1 and RA2 – Remote Amazon 1 and Remote Amazon 2; AD1, AD2, and AD3 – Arc of Deforestation 1, Arc of Deforestation 2, and Arc of Deforestation 3. Partial reproduction of Table 1 in Cecchini, Machado, Wendisch, et al. (2017).

The description of μ is especially relevant for studies assessing the effects of aerosol particles on clouds. Several observational and modeling studies suggested that the effects of aerosol loading on ϵ partially offset or enhance the aerosol second indirect effect, depending on the sign of the induced change in ϵ (e.g., Liu & Daum, 2002; M.-L. Lu et al., 2007; G. Martin et al., 1994; Pawlowska et al., 2006; Yeom et al., 2019; Y. Wang et al., 2021). Chen et al. (2016); Chen, Liu, et al. (2018) showed that the classical theory of condensational growth in an adiabatic parcel predicts an increase and a decrease in spectral width with increasing N_a and height, respectively, in the aerosol-limited regime, as well as spectral narrowing and broadening with increasing N_a and height, respectively, in the updraft-limited regime. The aerosol- and updraft-limited regimes are defined according to the magnitude of the sensitivity of N_c to N_a and w by considering condensational growth in an adiabatic parcel (Reutter et al., 2009). Relatedly, C. Lu et al. (2020) showed that correlations between ϵ and the volume-mean radius may have opposite signs depending on whether or not condensation/evaporation and activation/deactivation occur concomitantly in an adiabatic parcel where collision-coalescence is negligible. On the other hand, the laboratory studies of Chandrakar et al. (2016, 2018) showed that DSD width decreases as N_a increases considering condensation in a turbulent cloud, due to the reduction in supersaturation (S) fluctuations associated with a fast microphysics response.

Here we study the variability of ϵ (or μ) in observations and numerical simulations of growing convective cumuli, taking into account changes in the background N_a. Simulations using a LES model with bin microphysics contribute to the analysis of the mechanisms responsible for the variability of ϵ in cumulus clouds. Bulk-microphysics simulations illustrate the impact of improving the description of μ on the evolution of the simulated cloud.

2. Observations

2.1. Sampling Strategy and Instrumentation

During September–October 2014 (dry season), the High Altitude and Long Range Research Aircraft (HALO) performed a series of research flights over the Amazon, during the field campaign "Aerosol, Cloud, Precipitation, and Radiation Interactions and Dynamics of Convective Cloud Systems–Cloud Processes of the Main Precipitation Systems in Brazil: A Contribution to Cloud-Resolving Modeling and to the Global Precipitation Measurement" (ACRIDICON-CHUVA, Machado et al., 2014; Wendisch et al., 2016). The aircraft observation strategies and flight patterns performed during ACRIDICON-CHUVA included probing aerosol particles below cloud base, as well as measuring cloud properties near the base and the top of growing convective cumuli (Wendisch et al., 2016). Each flight focused on maritime, remote forest or deforested regions within or nearby the Amazon basin. To capture early stages of cumulus lifetime, the flights started close to local noon, when convection typically began in the region, during the campaign, and sampled clouds with no visible signs of precipitation below cloud base. A sensor system permanently installed at HALO (Basic Halo Measurement and Sensor System, BAHAMAS) provided basic aircraft position data and measurements of the 3-D wind field (Mallaun et al., 2015), pressure, temperature, humidity, etc.

Here we use data from six flights that sampled clouds in locations with contrasting aerosol conditions near the Amazon basin. Measurements of N_a were obtained with a butanol-based condensation particle counter (nominal cutoff particle size of 10 nm). In Wendisch et al. (2016), those flights are referred as "AC07", "AC09", "AC12", "AC13", "AC18" and "AC19", respectively. AC07, AC12 and AC13 measurements belong to the Arc of Deforestation, where biomass burning and anthropogenic sources generated relatively high average number concentrations of aerosol particles below cloud base ($N_a \sim 2000 - 4000$ cm^{-3}). AC09 and AC18 sampled clouds in remote locations over the unperturbed rainforest, with highly homogeneous surface conditions and $N_a \sim 800$ cm^{-3} below cloud base. Finally, AC19 was performed over the Atlantic ocean, near the mouth of the Amazon River, where N_a below cloud base was ~500 cm^{-3}. Table 1, reproduced from

Cecchini, Machado, Wendisch, et al. (2017), summarizes the main characteristics of these flights. For clarity, we rename flights AC07, AC12, AC13, AC09, AC18 and AC19 as "AD1", "AD2", "AD3", "RA1", "RA2" and "M1" respectively, as in Cecchini, Machado, Wendisch, et al. (2017). AD, RA and M stand for "Arc of Deforestation", "Remote Amazon" and "Maritime", respectively.

The Cloud Combination Probe (CCP) carried by HALO provided measurements of 1 Hz particle size distributions during the flights. The CCP employs a forward-scattering spectrometer, the Cloud Droplet Probe (CDP) (Lance et al., 2010), which measures particles with diameter between 2.5 μm and 46 μm, and a gray-scale optical array probe (CIPg, Cloud Imaging Probe, Baumgardner et al., 2001; Molleker et al., 2014), for particles with 25 μm < D < 960 μm.

Measurements of particle size distributions are highly susceptible to uncertainties in determining both sizes and concentrations, which in turn depend on the estimation of flow-related magnitudes, optical properties of the particles and characteristics of the instruments, among others (e.g., Brenguier et al., 2013; Lance et al., 2010). For instance, errors in estimating the flow velocity as well as the sample area affect estimations of the sample volume and, as a consequence, the particle number concentration. On the other hand, relatively small errors in the estimation of particle size and number concentration can have a significant impact on magnitudes derived from the particle size distribution, such as the liquid water content. Here, particle number concentrations under ambient conditions are derived from the CDP and CIPg measurements by applying a correction to the sample volumes that accounts for the compression of the air upstream of the instruments (Weigel et al., 2016).

The 1-Hz measurements analyzed here correspond to a spatial resolution of about 100 m, thus precluding analysis of smaller scale cloud variability. Unfortunately, there is a trade-off between the needs for studying small-scale particle distributions and for reducing random statistical fluctuations of the counting process. Assuming a Poisson probability distribution, the measured particle number concentration has to exceed 16 cm^{-3} and 0.04 cm^{-3}, for the CDP and the CIPg, respectively, to assure an uncertainty due to counting statistics of less that 5%. For this estimate we considered an aircraft velocity of 100 m s^{-1}, at a 1-Hz sampling rate, and reference sample volumes of 25 cm^3 and 10^4 cm^3, for the CDP and the CIPg respectively (Baumgardner et al., 2011, Table 1 therein). Uncertainties due to counting statistics are higher for size-binned particle number concentrations than for total number concentrations, especially for size intervals away from the mode. Additional analysis (not shown) indicates that the largest uncertainties associated with the counting process of the particles measured with the CIPg are found below the freezing level, while the largest uncertainties related to the particles measured with the CDP are found above the freezing level.

For more details about the instrumentation and flight patterns during ACRIDICON-CHUVA, the reader is referred to Wendisch et al. (2016).

2.2. General Characteristics of the Observations

Differences in surface characteristics among the AD, RA and M regions are correlated with differences in atmospheric thermodynamic conditions (Cecchini, Machado, Wendisch, et al., 2017). Figure 1 illustrates the potential temperature (θ), water vapor mixing ratio (q_v) and updraft speed (w) corresponding to in-cloud 1 Hz measurements during the six aforementioned flights. The data shown in Figure 1 was filtered by total number concentration of particles measured with the CDP larger than 16 cm^{-3} (i.e., counting statistics uncertainties smaller than ~5%), and w > 0 m s^{-1}, to focus on the ascending part of the growing clouds. Cloud base altitude increases moving from maritime to land deforested conditions, likely due to differences in surface sensible and latent heat fluxes (Braga et al., 2017; Fisch et al., 2004). While the dispersion of the θ measurements remains nearly constant with altitude, the spread of q_v at a given level increases with altitude, with up to 500% variation near ~5 km. The spread of q_v at a certain altitude is likely associated with the presence of subsaturated regions inside the cloud due to entrainment and mixing.

Figure 2 illustrates the vertical distribution of bulk properties of the particle size distributions for the 1-Hz measurements of each flight. Only measurements with total particle number concentration larger than 16 cm^{-3} for CDP and 0.04 cm^{-3} for CIPg are displayed in the upper and lower panels, respectively (the choice of these thresholds is based on counting statistics, as discussed in Section 2.1). Comparing M, RA and AD
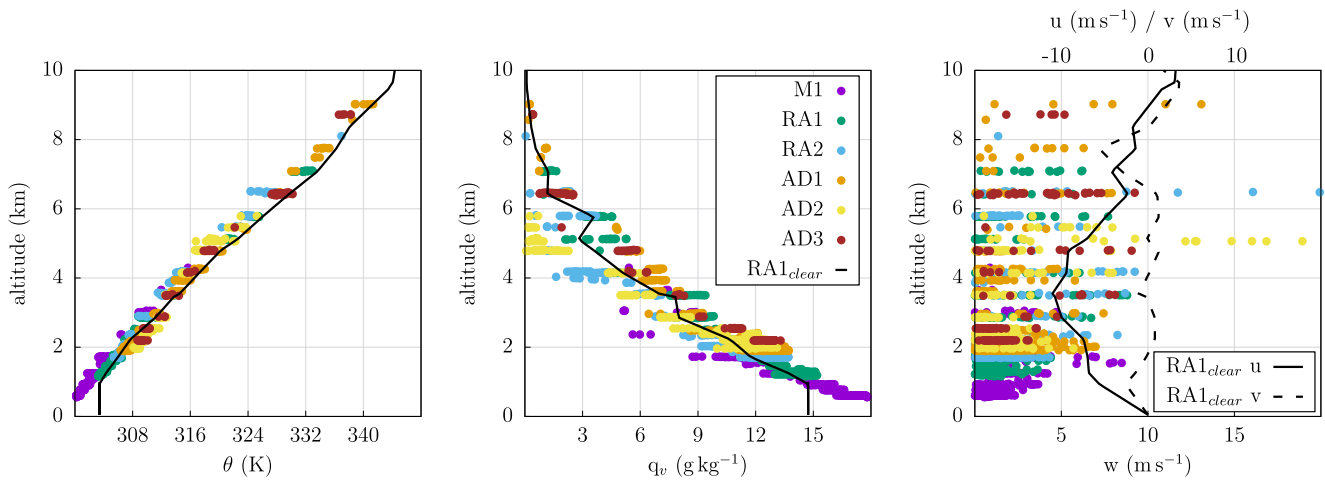
Figure 1. Vertical distribution of the measurements. Left panel: potential temperature (θ). Center panel: water vapor mixing ratio (q_v). Right panel: updraft speed (w) and averaged horizontal components of the wind from flight RA1 (u, v). Dots represent 1 Hz measurements filtered by $w > 0 \, \mathrm{m \, s^{-1}}$ and $N_c > 16 \, \mathrm{cm^{-3}}$. The black lines represent cloud-free averages for the RA1 flight.

flights, it is evident that N_a is positively correlated with the number concentration of particles measured with the CDP (Figure 2a), and negatively correlated with both the effective diameter of the CDP measurements (Figure 2b) and the number concentration of the CIPg measurements (Figure 2d), as expected based on the idea that high N_a limits warm rain production (Albrecht, 1989).

Water contents (i.e., mass concentrations) were calculated from the measured particle size distributions assuming spherical liquid droplets (Figures 2c and 2f). The adiabatic liquid water content derived from cloud-base measurements in each case is represented by short-dashed lines. The deviation of the water content derived from CDP measurements with respect to the adiabatic liquid water content (q_a) increases with altitude. Several factors might determine this behavior, including rain formation and entrainment-induced dilution and evaporation. An increase with altitude of the water content derived from CIPg measurements supports the former explanation. However, below the freezing level (note that the average location of the
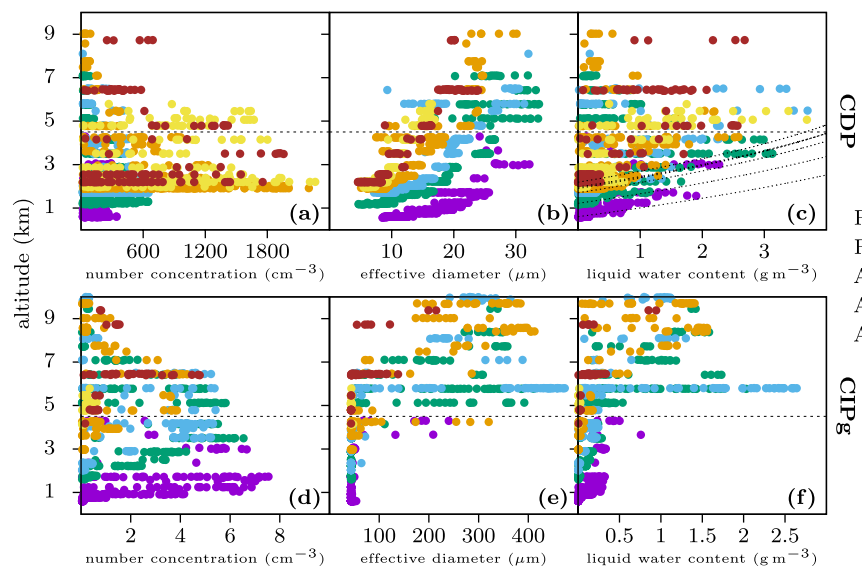
Figure 2. Vertical distribution of the particle number concentration, effective diameter and water content for Cloud Droplet Probe (2.5 μm $< D <$ 46 μm) and CIPg (25 μm $< D <$ 960 μm) 1-Hz measurements. The horizontal dashed line represents the average altitude of the 0°C isotherm. The short-dashed lines in panel (c) represent the adiabatic liquid water content estimated from cloud base measurements for each flight.

0°C isotherm is indicated by a horizontal dashed line at ∼ 4-km altitude), the values of the water content derived from CIPg measurements are too low (generally smaller than 0.5 $g\,m^{-3}$) to fully account for the differences between q_a and the water content of small particles measured with the CDP. Since larger particles have non-negligible fall velocities, evaluating rain production would require observations at several levels inside the clouds. ACRIDICON-CHUVA flights focused mainly on cloud tops and bases. The closer to cloud top the aircraft passed, the lower the chance of sampling precipitation particles coming from *higher* levels. Hence, the particles measured by CIPg (i.e., precipitation particles) were likely produced at, or very close to, the place of measurement. But the largest particles produced at this level may have already fallen, therefore not being captured in the measurements. In other words, in these observations, associating rain production with the differences between the water content derived from the CDP measurements and q_a is not straightforward. Nonetheless, the mere presence of large particles indicates that conversion from cloud droplets to rain/ice is, at least, one of the factors leading to deviation of the water content derived from the CDP measurements with respect to q_a.

Above the freezing level, there is a sudden increase in the water content and effective diameter of CIPg particles, especially for RA clouds. This coincides with an increase in the frequency of occurrence of aspherical particles, as reported by Cecchini, Machado, Wendisch, et al. (2017) for the same flights shown here. For the measurements where aspherical particles are present, the liquid water content calculated is likely overestimated, due to neglecting the differences between the densities and the shapes of liquid water and ice particles.

The following quantitative analyses focus on CDP measurements at $T > 0\,°C$. Besides decreasing the impact of errors related to the misestimation of the shape and density of ice particles, by focusing on cloud penetrations at $T > 0\,°C$, the overestimation of particle number concentrations due to ice shattering is likely minimized. Droplet splashing is also expected to remain relatively unimportant here, given the small effective diameter of CIPg particles at $T > 0\,°C$ (note that the probability of occurrence of droplet splashing increases with droplet size, e.g., Spanu et al., 2020). The CDP is less susceptible to particle shattering/splashing in general, compared to other spectrometers, owing to its aerodynamics design. Nevertheless, coincidence errors are still an important source of uncertainties for CDP measurements, which can lead to significant under-counting, oversizing and DSD broadening, especially in polluted clouds (Lance, 2012; Lance et al., 2010).

To improve the reliability of the DSD information obtained from CDP measurements (i.e., reduce the uncertainty related to counting statistics, as discussed above), we employ averages of the 1-Hz data over 100-m and 250-m height intervals. Although small aspherical particles (2.5 μm < D < 46 μm) were often detected in these measurements at $T > 0\,°C$ (Cecchini, Machado, Wendisch, et al., 2017), it is unclear whether they constitute large aerosols or ice particles. Additional instruments, such as CAS–DPOL (Cloud and Aerosol Spectrometer with Detector for Polarization, Baumgardner et al., 2001) would be required to distinguish between spherical and aspherical particles with D < 46 μm. CAS–DPOL measurements were collected during ACRIDICON-CHUVA, but their spectral resolution is lower than that of CDP. Classifying the particles according to their shape and analyzing the uncertainties involved in this process is beyond the scope of this study. For simplicity, we will refer to particles measured by CDP as "droplets".

2.3. Variability of the DSD Shape

Figures 3a1-3f1 show the average DSDs every 100 m vertically for each flight; height above cloud base h is represented by a color scale. Hereinafter, all observations are filtered according to a mask defined by $T > 0\,°C$, $w > 0\,m\,s^{-1}$ and $N_c > 16\,cm^{-3}$, derived from the discussion in Sections 2.1 and 2.2, and cloud-droplet water content (q_c) larger than 0.1 $g\,m^{-3}$, chosen to define the cloud boundaries. Droplet growth and spectral broadening with increasing h are noticeable for all flights. The broadest DSDs tend to contain multiple modes, which is likely a result of larger variability in individual 1 Hz DSDs at more advanced stages of cloud development. One of the most remarkable differences among DSDs from the different flights is the number concentration of smaller particles close to cloud base. At the lowest levels, as N_a increases, the number concentration of droplets with D <∼ 8 μm increases several orders of magnitude, thus resulting in broader DSDs near cloud base in the flights performed under polluted conditions compared to the flights in
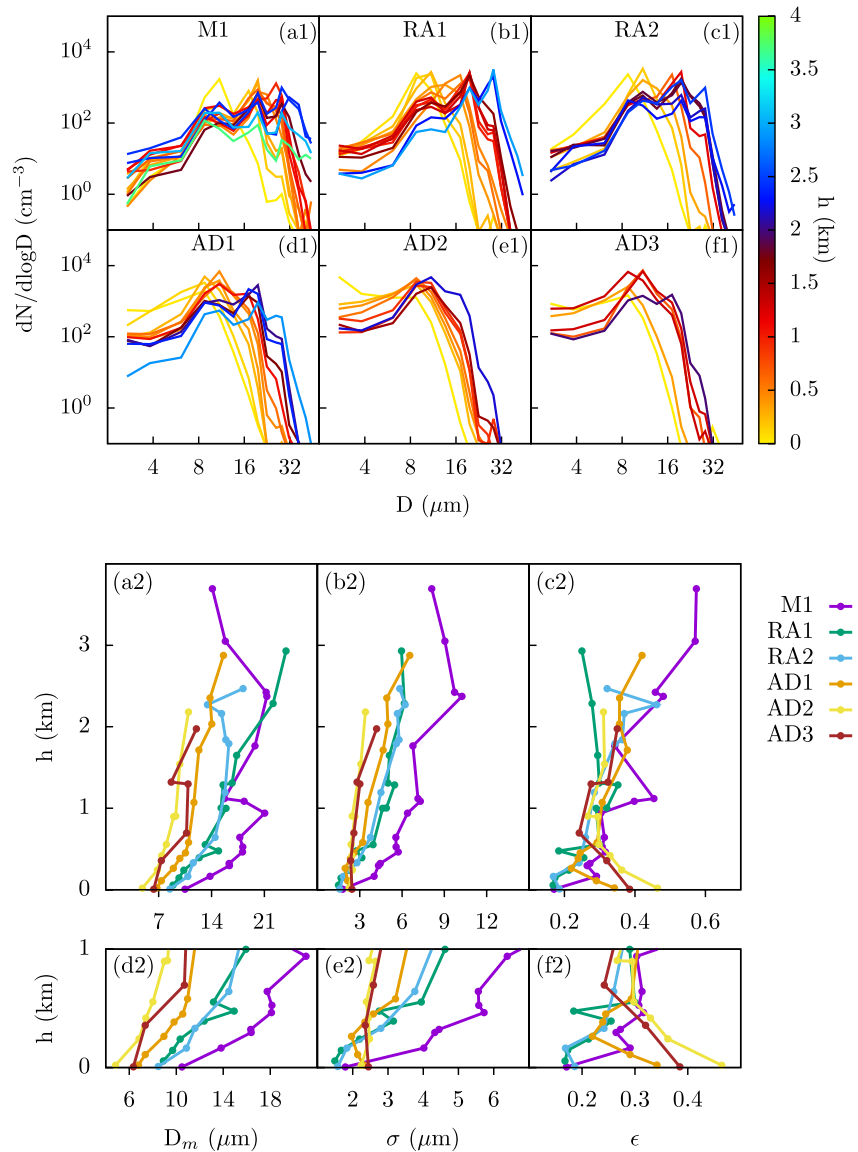
Figure 3. Upper panels (a1–f1): Average droplet size distributions (DSDs) every 100 m depth for each flight. The color scale represents height above cloud base (h). Lower panels (a2–f2): Mean diameter (D_m), standard deviation of the diameter (σ) and relative dispersion (ϵ) corresponding to the 100-m depth averaged DSDs. Panels (d2–f2) show a zoom on the lower 1 km above cloud base.

relatively clean environments. This is consistent with the results of Yeom et al. (2019), for observations of shallow cumuli over the Amazon during the local wet (low N_a) and dry (high N_a) seasons.

The relationship of DSD shape to N_a, w and h from ACRIDICON-CHUVA measurements was studied by Cecchini, Machado, Andreae, et al. (2017) and Braga et al. (2017). Here we extend their analysis to explore more details of the DSD variability. To provide some context, we first illustrate some aspects discussed by Cecchini, Machado, Andreae, et al. (2017). In their study, no strong correlation was found between w (in updrafts) and ϵ, therefore we initially focus on the variability of ϵ with respect to N_a and h.

Cecchini, Machado, Andreae, et al. (2017) showed that, for the flights in cleaner conditions, the DSD shape varies much more with h (which is considered as a proxy for cloud development) than for the polluted cases. They also concluded that the correlation between ϵ and N_a changes sign above $h \sim 500$ m. To complement their analysis, we show vertical profiles of D_m, σ and ϵ for the 100-m height average DSDs (Figures 3a2–3f2). Figures 3a2 and 3d2 show that D_m is negatively correlated with N_a for a given h. On the other hand, σ and

N_a are positively correlated near cloud base but negatively correlated at other levels (Figures 3b2 and 3e2). This behavior is associated with different rates of change of σ with h, depending on N_a, i.e., $\frac{\partial \sigma}{\partial h}\Big|_{N_a}$ decreases as N_a increases. A faster rate of increase of σ with h in clouds evolving in clean environments is consistent with more efficient DSD broadening and earlier rain initiation. Different trends of σ and D_m with increasing N_a explain large differences in ϵ among the flights close to the cloud base (Figure 3f2), with ϵ increasing by at least 30% from clean to polluted cases at the lowest level. Taking the derivative of $\epsilon(N_a, h)$ with respect to N_a, we see that the condition for $\frac{\partial \epsilon}{\partial N_a}\Big|_h$ to be positive (i.e., ϵ increases with increasing N_a at a given h) is that $\frac{\partial \sigma}{\partial N_a}\Big|_h > \frac{\sigma}{D_m}\frac{\partial D_m}{\partial N_a}\Big|_h$, which holds for $\frac{\partial D_m}{\partial N_a}\Big|_h < 0$ and $\frac{\partial \sigma}{\partial N_a}\Big|_h > 0$ at cloud base. Increasing ϵ with increasing N_a at cloud base is in agreement with Chen et al. (2016). As Chen et al. (2016) pointed out, DSD narrowing from condensational growth slows down as N_a increases in the aerosol-limited regime (Reutter et al., 2009), owing to the reduction in supersaturation compared to more pristine situations. However, their analysis applied condensational growth theory in an adiabatic parcel at the level of maximum S. Therefore, this mechanism cannot simply be extrapolated to other levels inside clouds, where additional mechanisms, such as collision-coalescence and entrainment/mixing, likely play important roles. In fact, for the observations analyzed here there is no clear relationship between the average ϵ at each level above cloud base and N_a (Figure 3c2).

2.3.1. Inferred DSD Broadening Mechanisms

To illustrate the variability of DSD shape in the observations further, we calculated the average of ϵ for 250-m intervals in h and intervals of 0.5 in q_c/q_a (Figures 4a1–4f1). Since the ACRIDICON-CHUVA flights intentionally avoided clouds with signs of precipitation below their bases, it is reasonable to regard q_c/q_a as a proxy for the adiabaticity of the cloud near cloud base, with q_c deviating from q_a in cloud areas that underwent mixing with the environment. The increase of ϵ with increasing N_a at cloud base discussed above is even more evident at high q_c/q_a values, i.e., within nearly undiluted cloud cores. In the lowest 250 m, ϵ increases by ~ 67% from the M and RA flights to the AD flights, for $q_c/q_a > 0.5$, while the increase is only ~ 10% for $q_c/q_a \leq 0.5$. Thus, it follows that the variability of the flight-averaged ϵ at cloud base described above is mainly determined by adiabatic processes, which likely explains the consistency with the analysis of Chen et al. (2016).

Figures 4a1-4c1 indicate that, for lower values of N_a (flights M1, RA1 and RA2), ϵ tends to increase as q_c/q_a decreases at most values of h, with ϵ being generally larger than 0.3 for $q_c/q_a < 0.5$. A similar tendency was reported by Yeom et al. (2019) for observations of Amazonian wet-season shallow cumuli. This behavior could be associated with DSD broadening due to the mixing of droplets undergoing different paths inside the cloud (i.e., the "eddy-hopping" mechanism, Cooper, 1989; Grabowski & Abade, 2017; Lasher-Trapp et al., 2005), specifically involving mixing of DSDs from parcels that experienced different levels of *dilution* (hence the lower ratio q_c/q_a). However, other processes can simultaneously decrease q_c/q_a and broaden the DSDs. In particular, as rates of collision-coalescence increase, which are mainly proportional to h for a given N_a (Freud & Rosenfeld, 2012), the DSD width increases and rain drops are eventually produced, leading to a decrease in q_c/q_a (keeping in mind q_c is the *cloud* not *total* liquid water content).

Overall, ϵ appears to be less correlated with q_c/q_a and h above cloud base for the AD flights (Figures 4d1–4f1), consistent with the delayed rain development in polluted clouds. Nevertheless, the DSDs are still fairly broad in these cases, with ϵ reaching values larger than 0.3 at most levels. A weak correlation between ϵ and q_c/q_a was also found by Yeom et al. (2019) for shallow cumuli developed under polluted conditions during the Amazonian dry season. A relatively uniform profile of ϵ above cloud base could result from compensation between the increase of ϵ by "eddy-hopping" DSD broadening (larger σ) and the decrease of ϵ by droplet growth (larger D_m). In these cases where the DSD broadening effect associated with collision-coalescence is weak, fairly large ϵ values could also be explained by in-cloud (often referred to as "secondary") droplet activation, which broadens DSDs toward smaller sizes. Since activation generally (though not always) increases ϵ but does not by itself modify q_c, this may potentially explain why the correlation between ϵ and q_c/q_a is
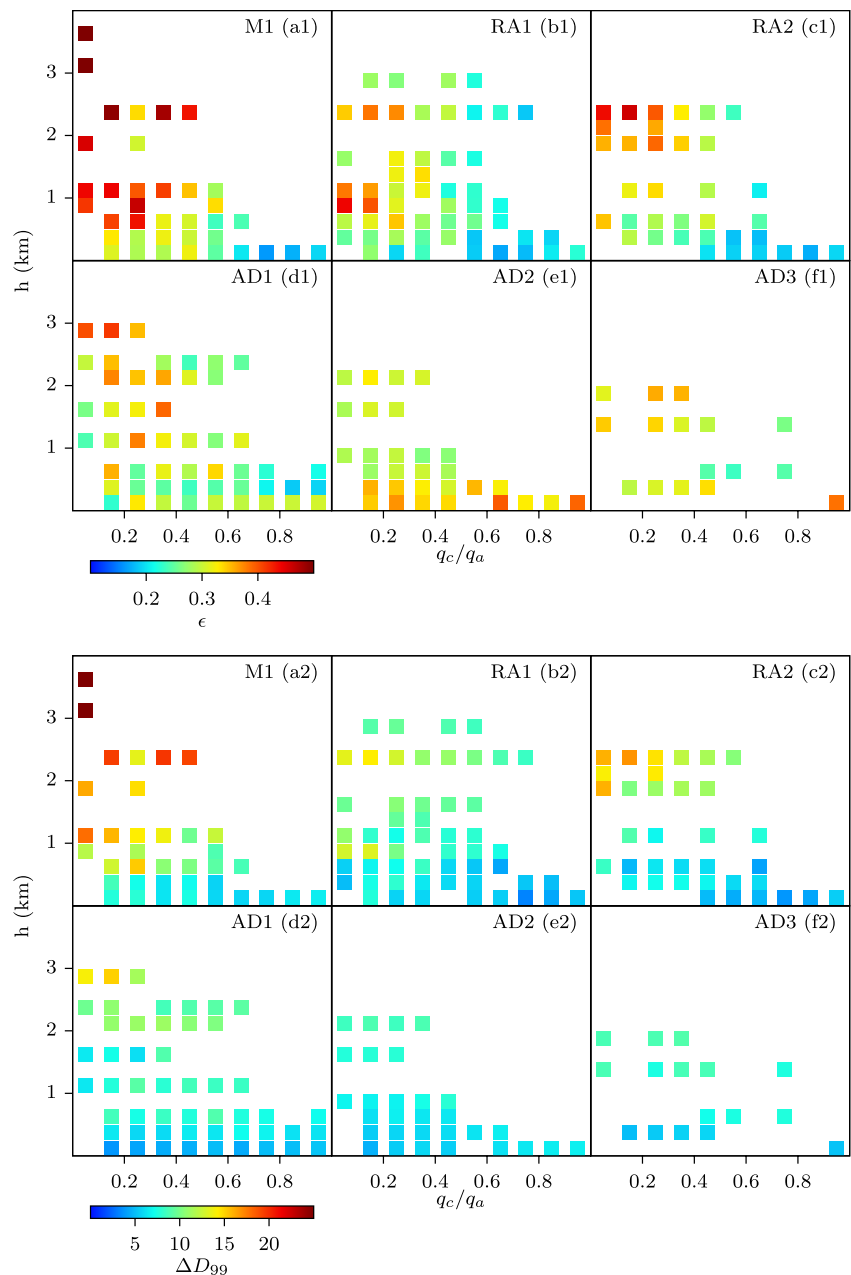
Figure 4. Averages of the relative dispersion (ϵ, a1–f1) and the difference between the sizes of the 99th and 50th percentiles (ΔD_{99}, a2–f2) of the droplet size distribution, for 250-m h and 0.5 q_c/q_a intervals in the observations.

weaker in the polluted compared to pristine clouds (where the latter is dominated by collision-coalescence). Note that secondary activation can occur in both diluted (i.e., through entrainment) and highly undiluted cloudy regions (Chandrakar et al., 2021; Hoffmann et al., 2015). According to the observations described by Yeom et al. (2019), for Amazonian shallow cumuli developed under polluted conditions, droplet activation in entrainment regions is more likely to occur compared to clouds in cleaner environments, presumably associated with an enhanced presence of large inorganic aerosols in the former case. Activation in highly undiluted cloudy regions depends on the transport of unactivated aerosol particles from cloud base and on the occurrence of high in-cloud S. In the cloud-core, S can increase with height above cloud base owing to both the acceleration of updrafts and the increase in the phase relaxation time scale associated with a reduction of N_c by collision-coalescence (e.g., Hernández Pardo et al., 2020; Pinsky & Khain, 2002). Analysis

of the relationship between N_c and the DSD shape for small intervals of q_c/q_a in the next section and the bin model simulations in Section 3.3 suggests the role of secondary activation on DSD broadening here.

These results show that neglecting changes in q_c/q_a hinders important details of the relationship between aerosol loading and DSD width. An increase in cloud dilution with h as a consequence of entrainment and mixing, as well as decreasing q_c via rain production, likely explains the relatively low number of observations with high q_c/q_a ($q_c/q_a > 0.5$) above cloud base. Although the existence of undiluted or nearly undiluted convective cloud cores has been reported by several observational studies (e.g., Khain et al., 2013, and references therein), if any undiluted cloud cores occurred in the cases here they would likely be missed since the clouds were mainly sampled by the cloud-top (or base) aircraft penetrations. In Section 3.3, the relationship $\epsilon - q_c/q_a$ is investigated, including for high q_c/q_a values above cloud base, based on idealized bin-microphysics simulations.

To focus on the right (large size) tail of the DSD, we calculated the difference between the sizes of the 99th and 50th percentiles of the DSD (ΔD_{99}). Figures 4a2–4f2 illustrate the distribution of the average values of ΔD_{99} as a function of q_c/q_a and h. Like ϵ, ΔD_{99} tends to be larger for smaller q_c/q_a, especially in the clean cases, but unlike ϵ, ΔD_{99} is also strongly correlated with h in all cases. Consistent with the well established effect of aerosols on warm rain production (Albrecht, 1989), the maximum values of ΔD_{99} are negatively correlated with N_a. ΔD_{99} is better correlated with ϵ in the M, RA1 and RA2 flights than in the AD flights, indicating that the distribution of ϵ in the former cases is associated with DSD broadening toward large drop sizes. In the AD flights, the trends of ΔD_{99} across the space of $(q_c/q_a; h)$ differ from those of ϵ. Furthermore, lower values of ΔD_{99} in the polluted flights, especially AD2 and AD3, suggest that the relatively large ϵ values across most of the space of $(q_c/q_a; h)$ for these cases are associated with broadening to small drop sizes, i.e., droplet activation.

In summary, the differences in the variability of ϵ and ΔD_{99} above cloud base between the observations in cleaner and polluted environments could be explained by two main broadening mechanisms: collision-coalescence and secondary droplet activation. Turbulent mixing of parcels that experienced different paths within the cloud (i.e., "eddy-hopping") also likely contributed to DSD broadening. In clean clouds, droplet growth by collision-coalescence may have dominated, increasing ϵ and ΔD_{99} with increasing h while simultaneously decreasing q_c/q_a through conversion to rain. In polluted clouds, the effect of secondary activation may have prevailed over collision-coalescence, as suggested by the highly uniform distribution of relatively large values of ϵ (~0.3) and relatively low values of ΔD_{99} (<~12 μm) at most values of h. To explore these hypotheses, in Section 3.3 we analyze the mechanisms determining the variability of DSD shape in bin microphysics simulations for different values of N_a.

2.4. Parameterization of the DSD Shape-Parameter

If the DSD follows a gamma distribution, then the ratio $\sigma/D_m \equiv \epsilon$ is related to μ ($\mu = \frac{1}{\epsilon^2} - 1$). Here we calculated μ using the method of moments, specifically from the zeroth, second and third moments, as in Cecchini, Machado, Wendisch, et al. (2017). Figure 5 illustrates the variations of μ depending on q_c/q_a and N_c, where N_c was averaged for intervals of $\Delta\mu = 5$ and $\Delta(q_c/q_a) = 0.1$, for visualization. As expected, the largest values of N_c are found at high q_c/q_a.

As discussed in the previous section, negative correlations between ϵ and q_c/q_a (positive correlations between μ and q_c/q_a) respond primarily to enhanced rain production in the clean cases, while in polluted clouds, rain production is limited and the variability of ϵ (μ) is less related to changes in q_c/q_a. The role of droplet activation is suggested by the relationship between N_c and μ. For q_c/q_a <~ 0.5 in the cleaner cases, and for most q_c/q_a values in the most polluted cases (AD2, AD3), μ is inversely related to N_c overall, consistent with the role of droplet activation in broadening the DSDs toward the left (small) side of the size spectrum. Note that collision-coalescence alone reduces μ as well as N_c, so the decrease of μ with increasing N_c for a given q_c/q_a is likely related to cloud droplet formation. Droplet activation at low q_c/q_a may occur in ascending diluted cloud areas, associated with the entrainment of aerosols and the local increase in S caused by the dilution-induced reduction of N_c, and also in undiluted regions of the cloud where
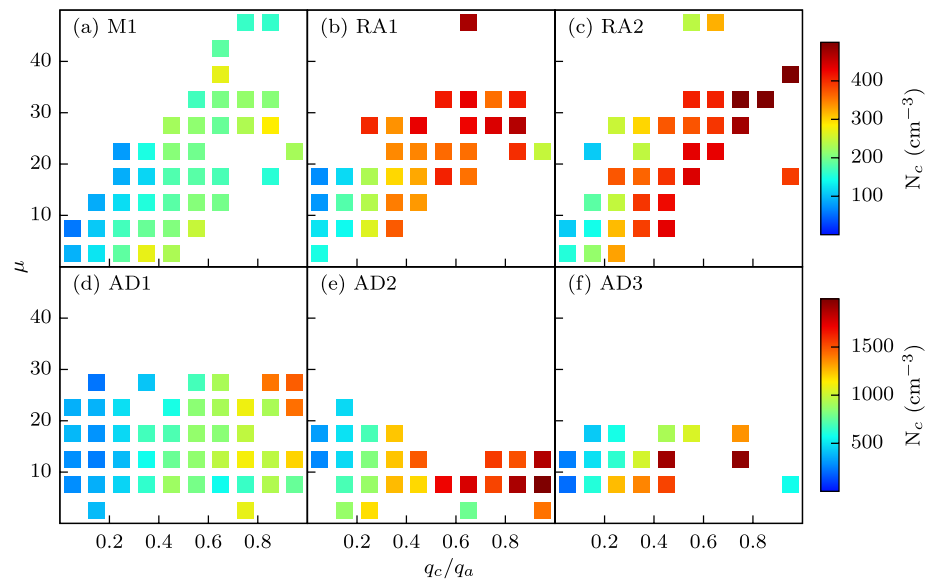
Figure 5. Averages of the cloud droplet number concentration (N_c) for intervals of five units of μ and 0.1 units of q_c/q_a in the observations.

q_c/q_a is reduced by rain formation. In the highly undiluted cloud core, collision-coalescence may increase S locally by decreasing N_c, resulting in the activation of aerosols ascending from cloud base (Hernández Pardo et al., 2020). Thus, there can exist favorable conditions for secondary droplet activation at low q_c/q_a, either related to dilution or to the reduction in q_c due to rain formation in undiluted areas, in both clean clouds and polluted clouds.

For the convective clouds sampled during ACRIDICON-CHUVA, bulk parameterizations that diagnose μ as inversely proportional to N_c are valid only for limited ranges of q_c/q_a and N_a ($q_c/q_a <\sim 0.5$ or $N_a > 3000$ cm^{-3}). In clean clouds, μ is positively correlated with N_c overall when the full range of q_c/q_a is considered. In order to analyze the potential for diagnosing μ from N_c and/or q_c/q_a, we fitted μ as a linear function of N_c (μ_1) and q_c/q_a (μ_2) separately, as well as a power law depending on both q_c/q_a and N_c simultaneously (μ_3). All fitting procedures were based on sets of 1-Hz observations, with fit parameters calculated separately for clean (M1, RA1 and RA2), polluted (AD2, AD3) and transition (AD1) aerosol conditions. Results are summarized in Table 2. Figure 6 shows scatter plots of parameterized μ against observed μ for each aerosol regime. For the clean cases, μ_2 is a better approximation to μ compared to μ_1, with an increase of $\sim 34\%$ in the root-mean-square error (RMSE) from μ_2 to μ_1. For polluted cases, μ_1 and μ_2 give similar RMSE. In all cases, no gain is obtained by considering both q_c/q_a and N_c in a power law functional relationship (μ_3). Therefore, we conclude that q_c/q_a is better for describing the variability of μ in these observations than N_c, at least for the functional relationships tested here. Additional tests using N_c/q_c (Liu et al., 2008) instead of N_c did not improve these results (not shown).

To represent the variations in the slope of the linear function that relates μ and q_c/q_a for different aerosol conditions, we derived μ_4, which varies the coefficients a' and b' as a function of N_a (see Table 2). For μ_4, the a' and b' coefficients were obtained by fitting a function (linear or power law, respectively) to the data set formed by the corresponding parameter (a or b, respectively) from each flight's μ_2 fits and N_a. Figure 7 illustrates the performance of this formulation compared to the parameterizations of Grabowski (1998); Rotstayn and Liu (2003); Thompson et al. (2008); Morrison et al. (2009) and Geoffroy et al. (2010) (Table 3). Despite the large scatter of μ_4 around the 1 : 1 line from the actual μ, it reduces the RMSE up to ~ 3 times compared to the other parameterizations. Figure 7 shows that the biggest improvements introduced by μ_4 are for larger values of μ. This is especially important for representing rain initiation in bulk models with autoconversion formulations that depend on μ. Averaging over relatively long distances (typically from tens to hundreds, even thousands of meters) often results in broader DSD compared to local ones (e.g., Khain

Table 2
Fitted Functions Relating the Shape Parameter (μ) With N_c and/or q_c/q_a for Each Aerosol Regime in the Observations: Clean ($N_a < 900\,\mathrm{cm}^{-3}$, Flights M1, RA1 and RA2), Transition ($N_a \sim 2500\,\mathrm{cm}^{-3}$, Flight AD1), and Polluted ($N_a > 3000$ cm^{-3}, Flights AD2 and AD3)

	Clean	Transition	Polluted
$\mu_1 = aN_c + b$	$a = 0.0335 \pm 0.0035$	$a = 0.0065 \pm 0.0011$	$a = -0.0014 \pm 0.0006$
	$b = 7.0585 \pm 0.9975$	$b = 9.4835 \pm 0.9443$	$b = 12.0728 \pm 0.6166$
	$RMSE = 8.63$	$RMSE = 5.76$	$RMSE = 3.23$
$\mu_2 = a\dfrac{q_c}{q_a} + b$	$a = 33.2747 \pm 1.5260$	$a = 8.8067 \pm 1.5240$	$a = -4.0482 \pm 1.2540$
	$b = 3.02492 \pm 0.6646$	$b = 10.0103 \pm 0.8889$	$b = 11.9921 \pm 0.4847$
	$RMSE = 6.45$	$RMSE = 5.79$	$RMSE = 3.19$
$\mu_3 = a\left[\dfrac{q_c}{q_a}\right]^b N_c^c$	$a = 27.5022 \pm 7.9480$	$a = 5.0548 \pm 3.4370$	$a = 15.2420 \pm 9.3820$
	$b = 0.8204 \pm 0.0489$	$b = 0.1258 \pm 0.0766$	$b = -0.0586 \pm 0.0687$
	$c = 0.0435 \pm 0.0485$	$c = 0.1763 \pm 0.0955$	$c = -0.0649 \pm 0.0795$
	$RMSE = 6.52$	$RMSE = 5.80$	$RMSE = 3.21$
$\mu_4 = a'\dfrac{q_c}{q_a} + b'$		$a' = m_a N_a + n_a \quad b' = m_b N_a^{n_b}$	
		$m_a = -0.0126 \pm 0.0006 \quad n_a = 40.9953 \pm 1.3880$	
		$m_b = 0.0125 \pm 0.0228 \quad n_b = 0.8449 \pm 0.2294$	
		$RMSE = 5.87$	

et al., 2015), therefore decreasing the likelihood of finding large values of μ in observations. Nevertheless, values of μ up to ~ 45 have been previously reported in the literature (e.g., Igel & van den Heever, 2017, and references therein), in agreement with the observations shown here.

In summary, results from the ACRIDICON-CHUVA observations provide interesting insights into the microphysical characteristics of Amazonian clouds. Specifically, we have shown that the spatial variability of DSD widths can be approximated as a function of q_c/q_a, especially in clean clouds, presumably due to the predominance of collision-coalescence which broadens the DSDs while also decreasing q_c. However, the lack of observations closer to the center of mass of the clouds limits the scope of these conclusions. In the next section, we discuss results from simulations of an idealized cumulus cloud to complement the observational analysis.

3. Simulations

Here we present the results of idealized simulations of a single convective cloud, using a LES configuration of the Weather Research and Forecasting (WRF) model (Skamarock et al., 2008). Unless specified, all model configurations are the same as the 3D simulations described in Hernández Pardo et al. (2020).

3.1. Model Description

The model horizontal domain comprises 40 km × 20 km ($x \times y$) with open lateral boundary conditions. The top of the model vertical grid is located at 10 km height, with a 3-km damping layer. The horizontal grid-spacing is 100 m, which is approximately equivalent to the displacement of HALO in 1 s (i.e., 1-Hz observations in Section 2). Therefore, the information from both the model and the observations refers to similar spatial scales. The vertical grid-spacing varies from ~115 m at the bottom of the

Table 3
Parameterizations for the Relative Dispersion (ϵ)/Shape Parameter (μ) Illustrated in Figure 7

Reference	Expression
Grabowski (1998)	$\epsilon = 0.146 - 5.964 \times 10^{-2} \ln\left(\dfrac{N_c}{2000}\right)$
Rotstayn and Liu (2003)	$\epsilon = 1 - 0.7e^{-0.003N_c}$
Thompson et al. (2008)	$\mu = \dfrac{1000}{N_c} + 2$
Morrison et al. (2009)	$\epsilon = 5.714 \times 10^{-4} N_c + 0.2714$
Geoffroy et al. (2010)	$\mu = 14.5q_c + 5.7$

Note. N_c and q_c represent the droplet number concentration in cm^{-3}, and the cloud water content in $\mathrm{g\,m}^{-3}$, respectively.
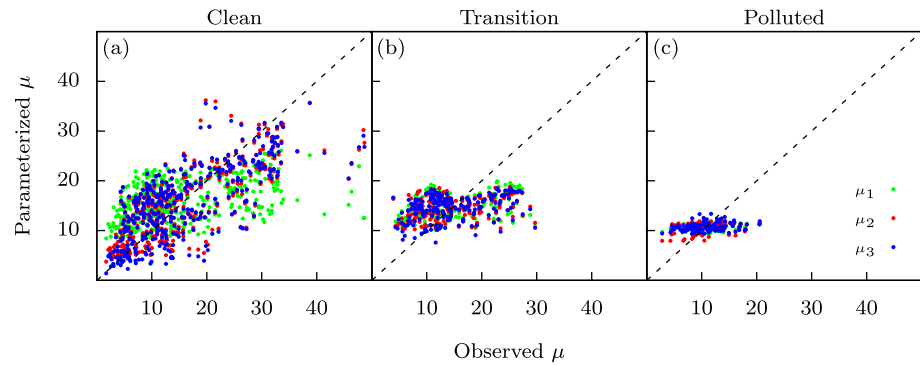
Figure 6. Scatterplots of observed versus parameterized shape parameter (μ) using the relationships specified in Table 2 for each aerosol regime: clean ($N_a < 900$ cm^{-3}, flights M1, RA1 and RA2), transition ($N_a \sim 2500$ cm^{-3}, flight AD1), and polluted ($N_a > 3000$ cm^{-3}, flights AD2 and AD3).

domain to ~50 m right below the damping layer. Convection is initiated by applying a + 3-K θ perturbation bubble (4-km horizontal- and 1.5-km vertical-axis length) at the center of the horizontal domain, at 1.5-km altitude. To spin up turbulent motions, small random perturbations (± 0.05 K) are added to the initial θ field in the lower one third of the vertical domain.

As initial conditions, we employ the averaged profiles of θ, q_v and the horizontal components of the wind (u and v) measured outside of the clouds (no cloud or rain drops present) in the RA1 flight. These profiles are represented by black lines in Figure 1. The initial values of θ and q_v were assumed to be constant with height from the surface to cloud base, to roughly mimic a well-mixed boundary layer. The initial u and v were assumed to be equal to zero at the surface, and increasing linearly from the surface to the cloud base.

We discuss results using two different microphysics schemes, the Tel Aviv University (TAU) two-moment bin microphysics scheme (Feingold et al., 1988; Stevens, Feingold, et al., 1996; Tzivion et al., 1987, 1989) and the two-moment bulk microphysics scheme of Morrison et al. (2009, M09 hereinafter).

The TAU scheme includes only warm phase processes. The DSD is divided into 35 mass-doubling bins with radii ranging between 1.56 μm and 5080 μm, approximately. To calculate the diffusional growth and
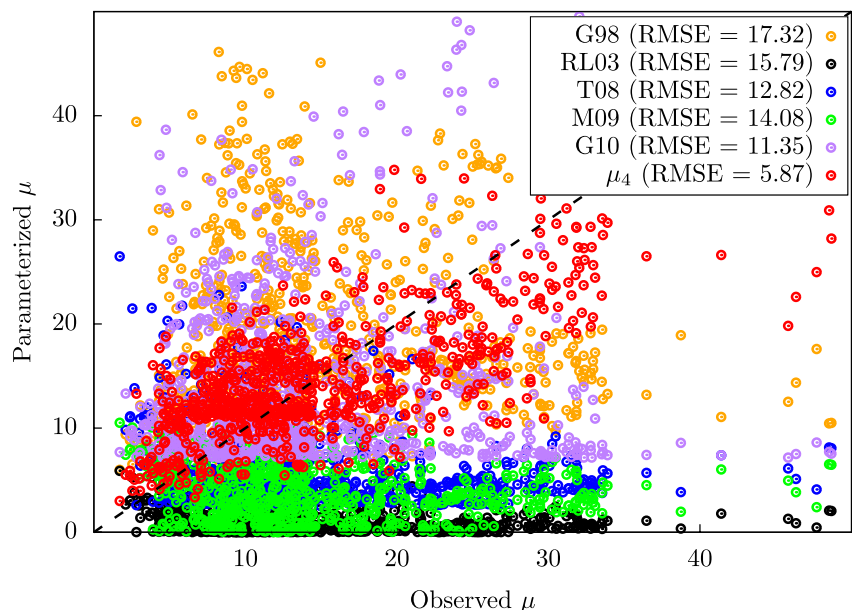

Figure 7. Scatterplot of observed versus parameterized shape parameter (μ) using the μ_4 relationship defined in Table 2 and the parameterizations specified in Table 3.

evaporation of droplets, the top-hat method of moments from Stevens, Feingold, et al. (1996) is employed. Solute and curvature effects on cloud droplet growth are neglected. The method of moments is used to compute mass and number mixing ratios in each size bin resulting from collision-coalescence (Feingold et al., 1988; Tzivion et al., 1987). Turbulent enhancement of collisions is not considered in the calculations of collision-coalescence here.

In the bin microphysics scheme, aerosol particles are assumed to be uniformly distributed throughout the model domain at $t = 0$, following a log-normal size distribution. According to ACRIDICON-CHUVA (flight RA1) measurements below cloud base, the geometric mean radius and geometric standard deviation are specified as 0.07 μm and 1.5, respectively. We assume that the hygroscopicity of the aerosols (κ) is equal to 0.1, based on previous studies of aerosol properties over the Amazon (Gunthe et al., 2009; S. T. Martin et al., 2010; Pöhlker et al., 2016). The hygroscopicity parameter here corresponds to the B parameter in Hudson and Da (1996), which is a particular case of the κ parameter in Petters and Kreidenweis (2007). The aerosol particle size distribution (PSD) is represented by a set of 19 bins, for radii between 0.0076 μm and 7.6 μm (Kogan, 1991). This way, the PSD is allowed to vary through activation and advection, but aerosol replenishment is neglected. Since aerosol particles in the larger-sizes tail of the PSD are removed after activation, there is generally less secondary activation for a given supersaturation compared to approaches that assume a fixed log-normal PSD without explicitly tracking aerosols. This prevents artificial enhancement of the collision-coalescence-activation feedback, whereby the decrease of N_c after collision-coalescence increases the supersaturation, which allows secondary activation, broadening the DSD and further strengthening collision-coalescence (e.g., Hernández Pardo et al., 2020).

Particles with radii larger than a critical radius (r_c), for a given temperature (T) and S, are instantaneously activated. According to Köhler theory:

$$r_c = \sqrt[3]{\frac{4A^3}{27S^2\kappa}} \qquad \text{with} \qquad A = \frac{2\sigma_s M_w}{RT\rho_w}, \qquad (2)$$

where σ_s is the surface tension of the solution/air interface, M_w is the molecular weight of water, R is the universal gas constant and ρ_w is the density of liquid water. All newly activated droplets are assumed to acquire a radius of ~1.5 μm, thus we do not explore the effects of large aerosol and giant cloud condensation nuclei.

The original bulk parameterization of M09 predicts mass and number mixing ratios of rain drops, cloud ice, snow and graupel/hail, but ice-phase processes are neglected in this study. Cloud droplets are represented by a gamma distribution, with $2 \leq \mu \leq 10$ depending on the (constant) value of N_c, following the observations of G. Martin et al. (1994) (Table 3). The condensation/evaporation rates are calculated assuming saturation adjustment. For parameterizing collision-coalescence processes (i.e., autoconversion, accretion and self-collection of rain drops), the method of Khairoutdinov and Kogan (2000, KK00) is employed. KK00 fitted power-law expressions for the rates of autoconversion, accretion and rain self-collection, depending on q_c, N_c, the rain water content (q_r) and the rain drop number concentration, based on bin-microphysics simulations of stratocumulus. Note that the method of KK00 does not depend explicitly on μ. In order to assess the effects of μ in the rate of collision-coalescence, we calculated offline rates of autoconversion, accretion and self-collection of both cloud droplets and rain drops following Seifert and Beheng (2006, SB06). In contrast to the KK00 scheme, the theoretical expressions derived by SB06 (and references therein) for the autoconversion and droplet self-collection rates do depend explicitly on μ.

The bin microphysics simulations are employed to extend our analysis of the observed $\mu - q_c / q_a$ relationship to include more levels inside the cloud, taking advantage of the information the model provides regarding microphysical process rates throughout the cloud. The bulk microphysics scheme is used to illustrate the effect of the fitted $\mu - q_c / q_a$ expression on the calculation of bulk processes rates, compared to the original M09 scheme.

3.2. General Characteristics of the Simulations

The nomenclature used for each simulation is shown in Table 4. Each simulation is identified by the type of microphysics scheme used (i.e., BIN or BULK), followed by one or two subscripts. For BIN, the subscript

Table 4
Nomenclature Used for the Simulations

Type		$N_a = 900 \text{ cm}^{-3}$	$N_a = 3000 \text{ cm}^{-3}$
Bin		BIN_C	BIN_P
Type	μ approach	$N_c = 500 \text{ cm}^{-3}$	$N_c = 1000 \text{ cm}^{-3}$
Bulk	μ as in M09	BULK_{OC}	BULK_{OP}
	$\mu = \mu_4 (\leq 20)$	BULK_{NC}	BULK_{NP}

represents the value of N_a assumed at $t = 0$ (C when $N_a = 900 \text{ cm}^{-3}$ and P when $N_a = 3000 \text{ cm}^{-3}$). For BULK, the first subscript indicates the approach employed to diagnose μ (O for the original M09 approach, N for the expression fitted from the observations here, i.e., μ_4). The second subscript indicates the specified constant droplet concentration N_c. We defined $N_c = 500 \text{ cm}^{-3}$ and $N_c = 1000 \text{ cm}^{-3}$ for BULK_C and BULK_P, respectively, based on the values of N_c predicted in the BIN simulations (see Figure 9). Whenever a subscript is missing, it means that we are referring to both options of the corresponding subscript. Note that, although activation is not predicted in the bulk scheme here, the effects of varying N_a are implicit in the value of N_c assumed in each case.

Figure 8 shows cross sections of q_c averaged over the y direction in simulations with $N_a = 900 \text{ cm}^{-3}$ and $N_a = 3000 \text{ cm}^{-3}$ (corresponding to $N_c = 500 \text{ cm}^{-3}$ and $N_c = 1000 \text{ cm}^{-3}$, respectively, for simulations using the bulk scheme), using the bin and bulk approaches, as specified in Table 4. Specific thresholds of the average q_r are represented by black contours in the figure. Hereinafter, we consider a diameter of $\sim 50 \, \mu m$ as the threshold separating cloud droplets from rain drops in the analysis of the BIN simulations, similar to the observations. As a result of having the same thermodynamic background, the shape and size of the clouds in different simulations are similar at each displayed time, at least up to $t = 12 \text{ min}$. From $t = 15 \text{ min}$ on, differences in rain production lead to changes in the structure of the clouds among simulations. Rain production is much faster in BULK than in BIN simulations. Nevertheless, in both BIN and BULK, changes in the time of rain initiation reveal the changes in N_c between cleaner and more polluted simulations. Average cross-sections of N_c in the BIN simulations are shown in Figure 9. Maximum values of N_c in BIN_P are at least two times the maxima in BIN_C. Correspondingly, rain develops earlier in the latter. At $t = 18 \text{ min}$, q_r exceeds 3 g m^{-3} in the upper half of the cloud in BIN_C, while values are generally less than 1 g m^{-3} in BIN_P. At $t = 15 \text{ min}$, a similar difference is evident between BULK_C and BULK_P.

Overall, the impact of changing the μ approach between BULK_O and BULK_N is very small (Figure 8). This is mostly explained by the fact that the KK00 method for estimating collision-coalescence (via autoconversion, accretion, and rain drops self-collection) does not depend on μ. In Section 3.4, we discuss the effect of μ on the rate of collision-coalescence diagnosed following SB06.

3.3. Variability of the DSD Shape in the Bin Microphysics Simulations

Figure 10 illustrates values of ϵ along a single cross-section through the center of the domain ($y = 0$-km) in the BIN_C and BIN_P simulations. Small oscillations in values of ϵ less than ~ 0.15 are evident inside the cloud at all times. This is likely related to advection, such as the non-conservation of integral quantities of the DSDs when binned quantities are advected individually in Eulerian models (Ovtchinnikov & Easter, 2009). However, the range of variation of ϵ is far greater than the amplitude of these oscillations. At earlier simulation times ($t \leq 12 \text{ min}$), larger values of ϵ ($> \sim 0.4$) are located near the base and the top of the cloud. As the cloud develops, values of $\epsilon > 0.4$ also appear in areas affected by entrainment and mixing near the lateral edges of the cloud.

Isolines of equivalent potential temperature (θ_e) equal to 343 and 346 K are represented by black continuous contours in Figure 10. Since θ_e is nearly conserved in moist adiabatic motion, it can be used to analyze the degree of dilution of parcels rising from cloud base (i.e., smaller θ_e implies greater dilution because mid-tropospheric θ_e is smaller than θ_e at cloud base). It is seen that, at earlier times of cloud development, most of the cloud area is encompassed by the 346-K isoline (see first and second rows in Figure 10). How-
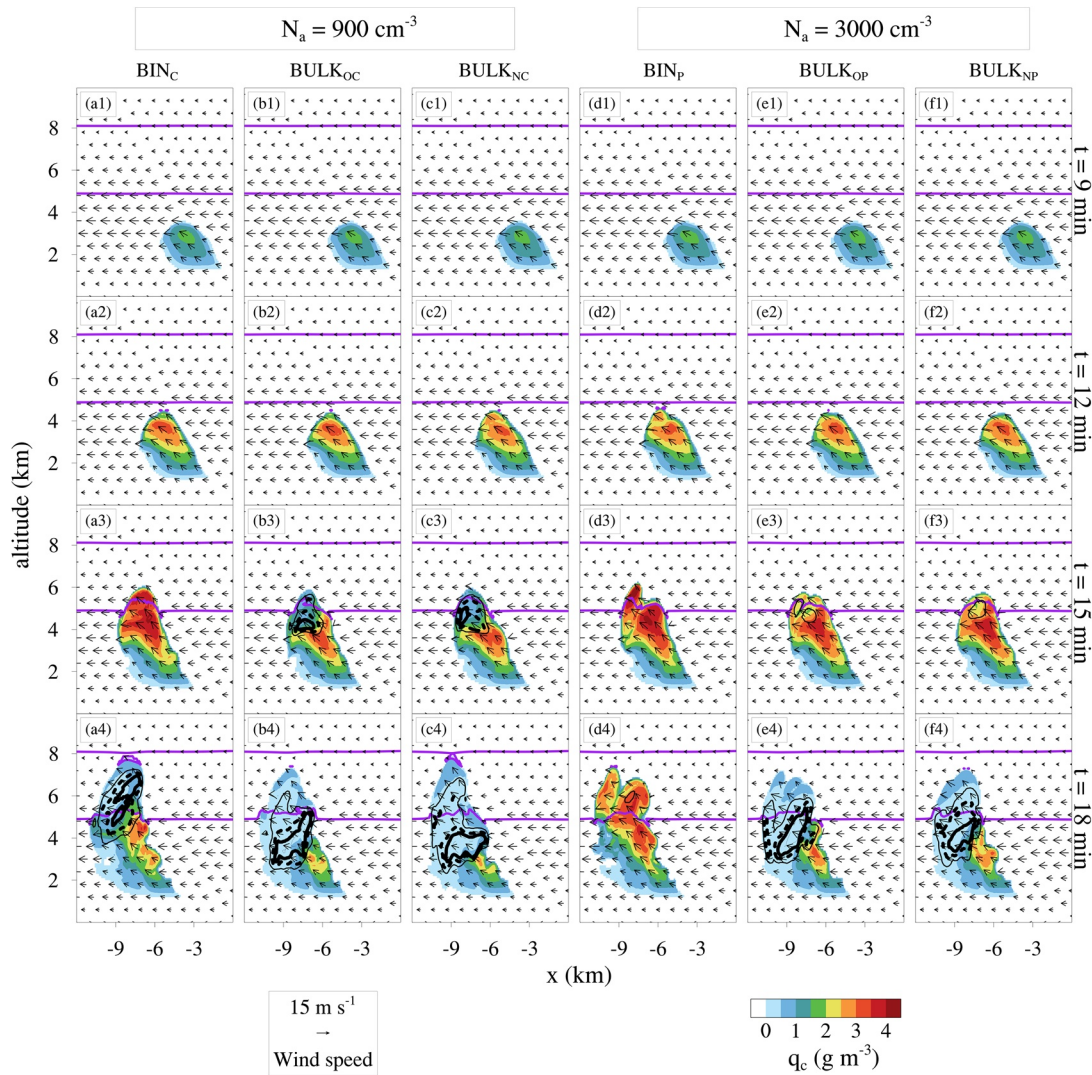
Figure 8. Cross sections of cloud water content (q_c, color scale), rain water content (q_r, thresholds of $1\,\mathrm{g\,m^{-3}}$, $2\,\mathrm{g\,m^{-3}}$ and $3\,\mathrm{g\,m^{-3}}$ are represented by thin-continuous-black contours, dashed-black contours and thick-continuous-black contours, respectively) and wind velocity (vectors) averaged over the y direction at various times (rows) in different simulations (columns). Averages in cloudy areas of the cross sections include only points at which the liquid water content is greater than $0.1\,\mathrm{g\,m^{-3}}$. The area enclosed between purple lines corresponds to average temperatures between $-10\,$C and $0°$C.

ever, at $t = 15$ min a considerable fraction of the cloud area on the downshear side of the cloud at altitudes between $\sim 2-4$ km has $\theta_e < 346$ K, indicating the effect of entrainment and dilution. Intense dilution in downshear areas of cumulus clouds has been previously reported in the literature (e.g., Rogers et al., 1985; Vaillancourt et al., 1997), related to the interaction of the thermal toroidal circulation with the surrounding wind shear (e.g., Damiani & Vali, 2007; Y. Wang & Geerts, 2013; Zhao & Austin, 2005). Relatively large values of ϵ (> 0.4) occurring very close to the position of the $\theta_e = 346$ K isoline at $t = 15$ min suggests the role of DSD broadening due to mixing of droplets that experienced contrasting levels of dilution.

Note that cloud "dilution" here refers to the mixing of the cloudy air with environmental air regardless of the ratio of the microphysical response timescale to the mixing timescale (i.e., homogeneous vs. inhomogeneous mixing). Several studies have shown that, depending on the initial shape of the DSD and the inhomogeneity of entrainment-mixing events, evaporation can have different effects on the DSDs (e.g., Bera et al., 2016; Guo et al., 2018; Korolev et al., 2016; Kumar et al., 2018; C. Lu et al., 2013; Luo et al., 2020; Pinsky & Khain, 2018; Pinsky, Khain, & Korolev, 2016; Pinsky, Khain, Korolev, & Magaritz-Ronen, 2016). However, LES models are not able to fully resolve the details of entrainment and mixing, since it depends
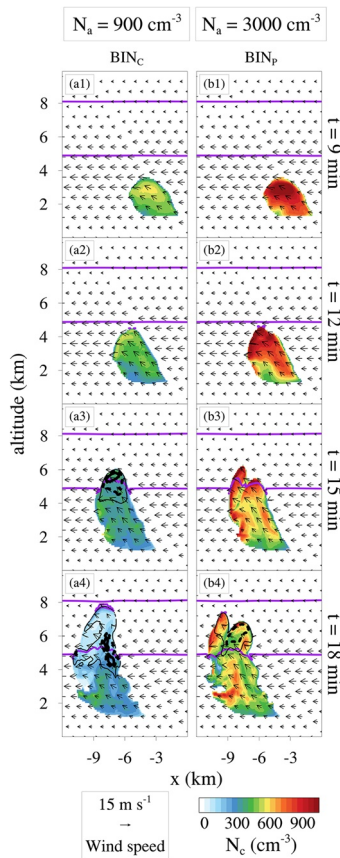
Figure 9. Similar to Figure 8 but for the average number concentrations of cloud droplets (filled contours) and rain drops (0.1 cm^{-3}, 0.3 cm^{-3} and 0.5 cm^{-3} black contours) in the BIN simulations.

on turbulent structures all the way down to the Kolmogorov scale. Kumar et al. (2018) found a strong dependence of the value of ϵ resulting after entrainment and mixing on the range of scales represented in Direct Numerical Simulations of a turbulent flow. The 10-Hz (i.e., ~10-m long flight paths) measurements reported by Yeom et al. (2019) suggest the predominance of homogeneous entrainment-mixing in Amazonian shallow cumuli. Nonetheless, independently of the direct effect of mixing on the DSDs, the decrease of N_c by dilution increases the phase relaxation time scale (excluding effects of secondary droplet activation), subsequently increasing the local supersaturation and, as a consequence, the condensational growth rate. The mixing of parcels that experienced different degrees of dilution, and therefore, different condensational growth rates, results in broader DSDs. A more detailed assessment of such effects in similar simulations (but neglecting the environment wind shear) is presented in Hernández Pardo et al. (2020).

At t = 18 min, most of the cloud area has θ_e < 346 K, indicating extensive dilution throughout the cloud, and the largest values of ϵ are located near the cloud top (~4 – 7 km altitude), consistent with rain initiation at higher levels inside the cloud. At this time, in BIN$_P$, the largest values of ϵ are mainly found within the most diluted areas (i.e., areas with θ_e < 343 K) near the cloud top. In contrast, at t = 18 min in BIN$_C$, large ϵ values (>0.5) are also common within the area encompassed by the 343-K isoline, i.e., relatively undiluted cloudy regions. This is consistent with enhanced rain production in the clean case, since collision-coalescence itself can lead to DSD broadening even in areas that are relatively undiluted. For a clean cumulus cloud simulated with a similar set-up as in this study, Hernández Pardo et al. (2020) showed that collision-coalescence is primarily triggered in nearly undiluted cloud cores associated with relatively high N_c compared to more diluted cloud regions, in agreement with Khain et al. (2013).

For consistency with the observational analysis, hereinafter we use only the first 15 min of the simulations, before the cloud rose above the freezing level, and consider only grid points with N_c > 16 cm^{-3}, q_c > 0.1 g m^{-3} and w > 0 m s^{-1}. To limit the effects of the oscillations in DSD shape mentioned above on the variability of ϵ and ΔD_{99}, we coarse-grained the model output by simply calculating the mean DSDs at cubic boxes consisting of $5 \times 5 \times 5$ grid points throughout the domain. Cloud-free grid points are neglected for averaging the DSDs in the boxes. Figure 11 illustrates the values of ϵ and ΔD_{99} corresponding to the box-mean DSDs over 500-m h and 0.1 q_c / q_a intervals. In both clean and polluted situations, ϵ tends to increase with decreasing q_c / q_a, except at cloud base (Figures 11a and 11c). The role of collision-coalescence and rain production on the distribution of ϵ in the $h - q_c$ / q_a space is inferred by the values of ΔD_{99}. Values of ΔD_{99} >~ 20 μm above 3-km depth (Figures 11b and 11d) coincide with the largest ϵ values (>0.5) in Figures 11a and 11c. This indicates that, as h increases, the DSDs are broadened toward the right side of the size spectrum, leading to rain production and thus decreasing q_c / q_a. Accordingly, the largest differences between the BIN$_C$ and BIN$_P$ simulations are found at the highest cloud levels. Less efficient conversion from cloud water to rain explains why large values of ϵ and ΔD_{99} (i.e., wide DSDs) occur over a wider range of q_c / q_a in BIN$_P$ compared to BIN$_C$.

The pattern of fairly large ϵ in the observations for the polluted cases, coinciding with smaller ΔD_{99} compared to the clean cases, suggests DSD broadening toward small sizes due to enhanced secondary droplet activation. This is to some extent reproduced by the model. Note that ϵ values reach similar maxima in BIN$_P$ and BIN$_C$. In contrast, the maximum value of ΔD_{99} is smaller in BIN$_P$ than in BIN$_C$, and the height above cloud base h at which ΔD_{99} surpasses a certain value (e.g., 20 μm) increases from BIN$_C$ to BIN$_P$. This indicates that, at a given h, the contribution of larger droplets to ϵ decreases as N_a increases. Therefore, an increase of ϵ is mostly associated with an enhancement in the amount of small drops in high-N_a conditions,
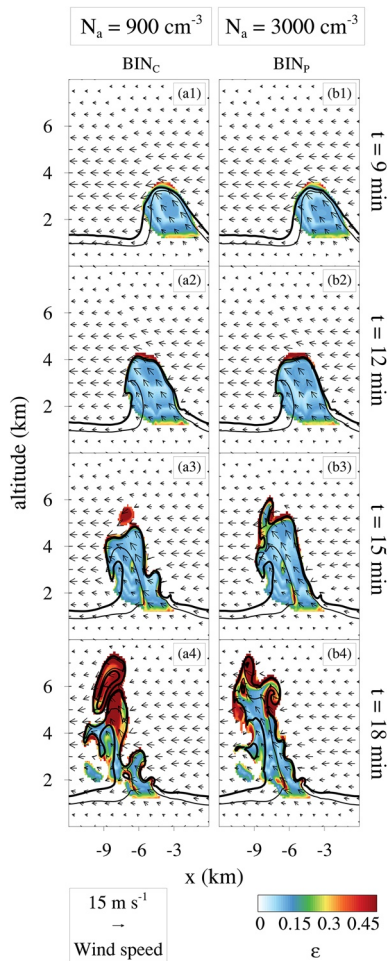
Figure 10. Relative dispersion (ϵ, color scale) and wind velocity (vectors) at the $y = 0$ km cross-section in the BIN simulations. The thick and thin black contour lines represent isolines of equivalent potential temperature (θ_e) equal to 343 and 346 K, respectively.

in agreement with the observations. Additional analysis for individual simulation times (not shown) indicates that this mechanism is accentuated near cloud top, which likely explains its occurrence in the observations. On the other hand, the values of ϵ at cloud base in the simulations are insensitive to N_a, in contrast to the observations. This might be related to neglecting the solute and curvature effects in the condensation calculations, or assuming the same PSD shape (i.e., same geometric mean radius and geometric standard deviation, only varying the total number concentration) and κ for aerosol in both BIN_C and BIN_P. As shown by Pöhlker et al. (2016, 2018), changes in N_a over the Amazon are associated with different aerosol sources, and thus likely the aerosol particle populations have different size and chemical properties as well. A potentially key factor is that all new drops are assumed to have a radius of ~1.5 μm (i.e., the smaller bin of the DSD in the model). This may limit the sensitivity of the DSD to changes in the PSD shape in the model.

3.3.1. DSD Broadening Mechanisms

Figure 12 shows the average rate of collision-coalescence (CCrate), activation (ACTrate) and condensation (CONDrate) as a function of h and q_c/q_a in the bin simulations, considering model results up to $t = 15$ min. CCrate approximately represents the total number concentration of droplets ($D < 80$ μm) undergoing collision-coalescence per second. In practice, CCrate is calculated as the sum of the loss term of the smaller 14 bins of the DSD, due to collision-coalescence. ACTrate is the ratio of the total number concentration of droplets activated per second to N_a. CONDrate indicates the rate of change of the mean droplet size due to diffusion of water vapor to/from cloud droplets. It is seen that CCrate behaves similarly in the BIN_C and BIN_P simulations, with a maximum at large q_c/q_a values and relatively high h, but the magnitude is much larger in BIN_C than BIN_P. Examination of CCrate provides further support for the mechanism mentioned earlier, in which the increase in rain production in nearly undiluted cloud core regions leads to the occurrence of broader DSDs at low q_c/q_a values, depending on h. As collision-coalescence increases with increasing h, the consequent reduction in N_c increases S, subsequently enhancing droplet activation and condensational growth too. Despite the differences in the intensity of CCrate between BIN_C and BIN_P, large ACTrate and CONDrate values occur over a wide range of
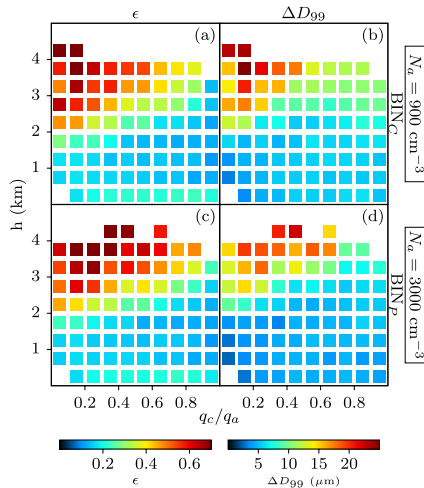
q_c/q_a above $h \sim 3$ km, in both simulations. This suggests the role of cloud dilution, in addition to collision-coalescence, in decreasing N_c and therefore increasing S in the upper areas of the cloud. In general, large values of ACTrate and low values of CCrate in BIN_P are consistent with an enhanced contribution of smaller droplets to increases in ϵ in this case, as discussed above. Large values of CONDrate at specific locations within the cloud also contribute to creating the conditions for "eddy-hopping" DSD broadening by accentuating differences in droplet size among different parcels (e.g., Hernández Pardo et al., 2020).

Our analysis of the simulations supports the idea that ϵ increases with decreasing q_c/q_a either due to entrainment, dilution and mixing near the cloud edges, and/or rain production in nearly undiluted cloud cores. However, the dependence of ϵ on h is stronger in the simulations than in the observations (Figure 4 vs. Figure 11), with ϵ being larger above and smaller below ~ 1 km in the model than in the observations. The underestimation of ϵ at low h in the model could be associated with an under-representation of entrainment and dilution during early cloud stages and at low levels above cloud base. Mixing of parcels undergoing different condensation/activation paths can lead to DSD broadening in clouds (Cooper, 1989; Grabowski & Abade, 2017; Lasher-Trapp et al., 2005). Thus, increased mixing at levels near cloud base could improve comparison with the observations. On the other hand, the overestimation of ϵ at $h > 1$ km in the model could be related to excessive collision-coalescence, which leads to DSD broadening toward large droplet sizes and also toward small sizes through its feedback on the rate of droplet activation (i.e.,

Figure 11. ϵ and ΔD_{99} corresponding to mean droplet size distributions (DSDs) every $5 \times 5 \times 5$ grid-points boxes in BIN_C and BIN_P simulations. For better visualization, displayed values correspond to averaged ϵ and ΔD_{99} at each 500-m h and $0.1\ q_c/q_a$ intervals. Note that averaging ϵ and ΔD_{99} is not equivalent to averaging the DSDs prior to deriving ϵ and ΔD_{99}.

collision-coalescence decreases N_c, thus increasing S). An underestimation of the supersaturation maximum at cloud base may cause an overestimation of the amount of unactivated aerosols in the cloud core, which in turn may lead to an overestimation of the rate of in-cloud activation. As shown in Morrison and Grabowski (2008), increasing the vertical grid spacing from 2 to 50 m can reduce the cloud-base supersaturation maximum by almost one-half. This is more critical in polluted conditions, where the maximum supersaturation occurs closer to the cloud base, because of the shorter phase relaxation time scale compared to cleaner clouds. The generation of high supersaturation at cloud top due to the separate advection of temperature and water vapor (Grabowski & Morrison, 2008; Stevens, Walko, et al., 1996), with contributions from evaporation as the cloud edge advects into non-cloudy grid cells (Hoffmann, 2016), may enhance in-cloud droplet activation as well. However, similar to Hernández Pardo et al. (2020), this mechanism appears to be negligible here, since sharp peaks of the supersaturation are not systematically evident at cloud-top in these simulations. Scarce measurements in nearly undiluted cloud areas might be another factor explaining differences in ϵ between the model and observations.

Although physical processes typical of cumulus clouds explain the clear correlation between DSD shape and the degree of deviation of q_c from q_a, at least for low aerosol conditions, expressing ϵ (or μ) as a function of q_c/q_a involves significant uncertainties. Results from the BIN simulations suggest that the correlation between μ and q_c/q_a varies with h. Nevertheless, considering the relationship of μ with q_c/q_a as well as with N_a found in the observations represents an improvement compared to previous parameterizations commonly used in double-moment bulk schemes that are based on N_c or q_c only (see Section 2). In the following, we discuss the impact of including the relationship $\mu_4 = f(q_c/q_a, N_a)$ in the bulk scheme of M09, for analogous simulations as in the BIN tests above.
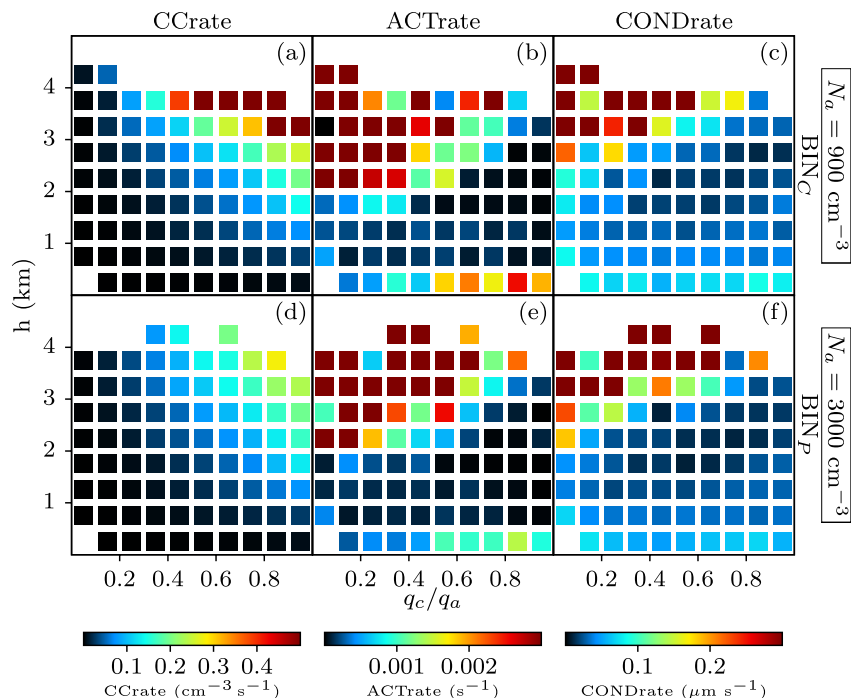

Figure 12. Similar to Figure 11 but for the rate of collision-coalescence (CCrate), activation (ACTrate) and condensation (CONDrate).
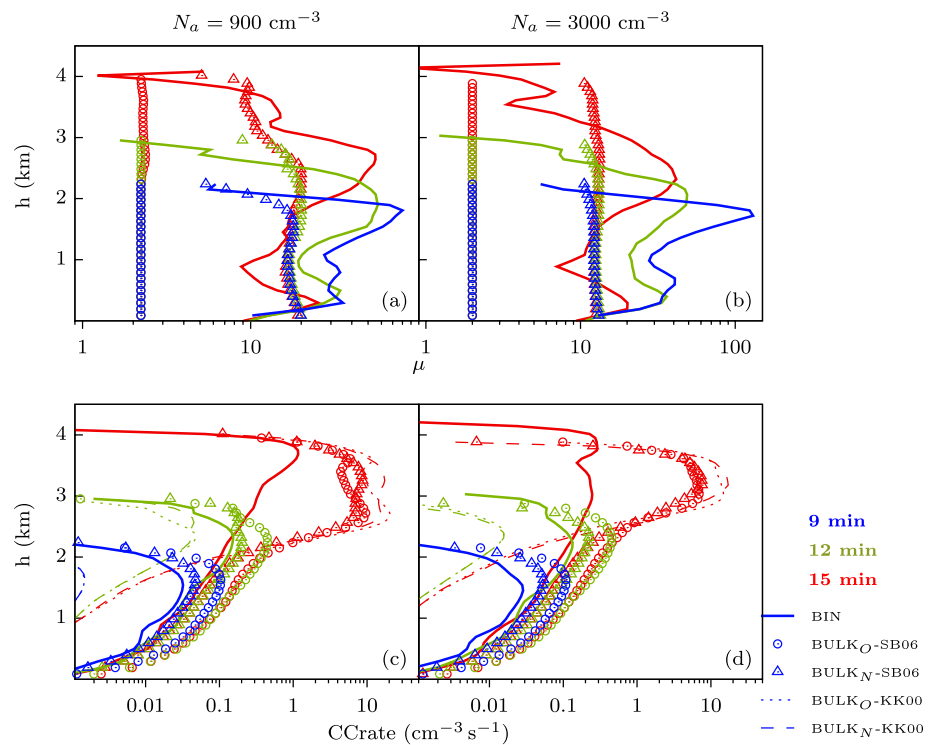
Figure 13. Mean profiles of the shape parameter (μ) and the collision-coalescence rate (CCrate) in BIN and BULK simulations.

3.4. Impact of Changes in the Shape Parameter in the Bulk Microphysics Simulations

In Section 3.2, we showed that BULK simulations, based on the double-moment microphysics scheme of M09, differed significantly from BIN simulations. Specifically, we showed that rain production was more efficient in BULK than in BIN.

The mean profiles of μ from each simulation are illustrated in Figures 13a and 13b. It is seen that in the BIN simulations μ is generally larger than in $BULK_O$, which uses the default formulation for μ following G. Martin et al. (1994), thus representing narrower DSDs. In $BULK_O$, μ is inversely related to N_c. Since N_c is nearly constant in the default scheme of M09 (small variations in N_c may occur within a single time-step due to adjustments during conservation checks), μ has almost no intra-cloud variations in the $BULK_O$ simulations. This shows that, although the $\mu - N_c$ relationship employed by M09 might represent inter-cloud variability in certain situations (as it follows from the observations reported by G. Martin et al., 1994), it is inconsistent with the intra-cloud variability found in the observations and BIN simulations here. Results from our analysis of the observations and BIN simulations indicate that variations of μ within a single cloud can be larger than the broader variations among clouds developed in different environments.

As discussed in Section 2.4, the relationship $\mu = f(q_c/q_a, N_a)$ employed in $BULK_N$ (i.e, μ_4) provides a better approximation of the intra-cloud variability of μ than previous parameterizations. Accordingly, Figures 13a and 13b indicates that μ in $BULK_N$ is generally closer to the BIN profile compared to $BULK_O$, although the upper bound of 20 defined for μ in these tests prevents it from replicating the larger values found in BIN (μ is limited to a maximum value of 20 to prevent underflow/overflow problems when running the code). Besides being closer to BIN in general, μ_4 reproduces the decrease in μ (increase in DSD width) toward the cloud edges, as in the BIN simulations. For instance, the mean profile of μ in $BULK_N$ simulations consistently represents the decrease of μ at cloud top at all times.

Figures 13c and 13d shows average profiles of CCrate in the simulations. In the bulk scheme, CCrate was calculated as the number of cloud droplets undergoing collision-coalescence (i.e, including the effects of autoconversion, accretion and self-collection of *cloud droplets*) according to the approaches of KK00 and

SB06. The former is the default method employed in M09 and was used to update the microphysical variables in the simulations, while the latter was used only as a diagnostic. Note that the method of KK00 for parameterizing collision-coalescence considers a threshold diameter separating cloud droplets and rain of 50 μm, while in SB06 this threshold is 80 μm. In BIN, CCrate was diagnosed from the total number of colliding droplets smaller than 80-μm diameter. We verified that increasing the threshold diameter from 50 μm to 80 μm has negligible impact on CCrate for $t \leq 15$ min in BIN simulations, due to the predominance of small droplets in the early stages of cloud development.

In both the BIN and BULK simulations, the maximum CCrate occurs near the top of the cloud, coinciding with the maximum liquid water content ($q_c + q_r$, Figure 8). However, CCrate values obtained with the method of KK00 in BULK differ significantly from CCrate in BIN. This is expected, considering that the method of KK00 was originally developed for the specific case of stratocumulus clouds. Figures 13c and 13d evidence that the onset of collision-coalescence calculated according to KK00 is delayed with respect to BIN, with CCrate-KK00 being more than one order of magnitude smaller than CCrate-BIN at $t = 9$ min. Afterward, CCrate-KK00 accelerates, exceeding CCrate-BIN by more than one order of magnitude at $t = 15$ min. Furthermore, KK00 leads to higher vertical gradients of CCrate compared to BIN. These results highlight the importance of carefully considering the case-dependency of the parameterizations of microphysical processes in bulk schemes. Changing the approach for diagnosing μ does not significantly affect CCrate-KK00, as expected, since the representation of collision-coalescence processes in KK00 has no explicit dependency on μ. Similar results were obtained using the expressions derived by Kogan (2013) (not shown), a cumulus version of the parameterization of KK00.

In contrast to KK00, CCrate diagnosed using the method of SB06 reproduces the vertical distribution of collision-coalescence in the BIN simulations (Figures 13c and 13d). Nevertheless, CCrate-BIN is generally lower than CCrate-SB06, consistent with the larger values of μ (i.e., narrower DSDs) in BIN compared with BULK simulations. Increasing μ from BULK_O to BULK_N improves the estimation of CCrate-SB06, except between $\sim 3 - 4$ km above cloud base at $t = 15$ min, where the intense collision-coalescence derived from KK00 already developed rain in the BULK simulations (Figure 8). These results indicate that, if microphysical fields in BULK were online with the collision-coalescence rate estimated from the approach of SB06, improving the description of μ would lead to a better representation of rain initiation. Online calculations of CCrate using SB06 are not shown here because applying this approach requires varying N_c, for consistency with the physical considerations used to derive its expressions for autoconversion, accretion and droplet self-collection. Varying N_c within the scheme of M09 in WRF is beyond the scope of this study.

4. Conclusions

This study addressed the variability of DSD shape in observations and numerical simulations of warm cumulus clouds, with emphasis on the relationship between DSD broadening mechanisms on the background aerosol particle number concentration (N_a). Factors impacting the spatial distribution of the spectral dispersion of droplets in cumulus clouds, especially height above cloud base, adiabaticity and aerosol loading (Khvorostyanov & Curry, 1999, 2008), were explored in the observations and the bin microphysics simulations. We discussed prospective relationships for diagnosing the shape parameter (μ) of the droplet gamma size distribution for use in bulk microphysics models.

Relatively clean clouds ($N_a < 900$ cm^{-3}), observed over maritime or remote rainforest regions, showed a strong relationship between the DSD relative dispersion (ϵ) and the ratio of the cloud water content (q_c) to the adiabatic liquid water content (q_a). The bin microphysics simulations indicated that this behavior is primarily caused by collision-coalescence, which simultaneously increases ϵ and decreases the q_c through rain production. In the observations, the strengthening of collision-coalescence was indicated by an increase in the large-sizes tail of the DSDs with increasing height above cloud base. At lower levels and $q_c/q_a <\sim 0.5$, DSDs with relatively large relative dispersion ($\epsilon \sim 0.3 - 0.4$) and small large-sizes tails (indicated by the difference between the sizes of the 99th and 50th percentiles of the DSD, $\Delta D_{99} \sim 12$ μm) may have been mainly associated with high activation and condensation rates in diluted air parcels near the cloud edges. Dilution reduces the cloud droplet number concentration (N_c), and therefore increases the supersaturation (S) as the entrained air rises within the updraft, leading to DSD broadening and thus increasing ϵ after mixing with

less diluted parcels from the cloud core, where droplets may have experienced lower S (Hernández Pardo et al., 2020). This way, the inverse relationship between ϵ and q_c/q_a can be sustained in both diluted and nearly undiluted regions of clean clouds.

Polluted clouds ($N_a > 2000 \text{ cm}^{-3}$), observed over deforested regions, showed a smaller variability of DSD width, with a weaker dependence of ϵ on q_c/q_a. This finding is consistent with a lower rate of collision-coalescence and delayed rain production in polluted clouds compared with cleaner clouds. Large ϵ values ($\sim 0.3 - 0.4$) coinciding with small tails ($\Delta D_{99} \sim 8 \ \mu$m) occurred at most levels and values of q_c/q_a in the observations. This was likely caused by enhanced droplet activation throughout the cloud and DSD broadening after mixing of air parcels undergoing different paths inside the cloud. A similar effect occurred in the bin simulations, with a tendency to maintain large ϵ values and to decrease the size of the DSD tail for higher N_a, associated with an increase in the droplet activation rate and a decrease in droplet growth rate by collision-coalescence.

In general, the variability of ϵ was larger in the bin simulations than in the observations. An inverse relationship between ϵ and q_c/q_a was evident at most levels above cloud base, not only in the simulation of the cleaner cloud ($N_a = 900 \text{ cm}^{-3}$) but also of the polluted one ($N_a = 3000 \text{ cm}^{-3}$). Moreover, while the slope of the $\epsilon - q_c/q_a$ relationship did not change significantly with height above cloud base in the observations, it notably increased (in absolute value) with height above cloud base in the simulations. One factor that could impact this comparison is the fact that all measurements performed above the cloud base in the observations corresponded to levels near cloud top. Nevertheless, additional analysis showed that a pronounced increase of this slope with height above cloud base also occurred when only the upper 500 m of the cloud at each simulation time was considered. Therefore, this behavior suggests that spectral broadening mechanisms may be too efficient in the model compared to the observations. An overestimation of the spectral broadening at higher levels above cloud base in the simulations may be related to excessive collision-coalescence, as well as to spurious mechanisms such as the numerical diffusion in mass/size space associated with the combination of condensational growth and advection in physical space (Hernández Pardo et al., 2020; Morrison et al., 2018). Additionally, an underestimation of entrainment and dilution at early stages of cloud development and low levels above cloud base could explain narrower droplet spectra at the lower levels in the model compared to the observations. Narrower spectra at lower levels and broader spectra at upper levels lead to a larger variation of ϵ with height above cloud base in the model compared to the observations. Future research including the representation of mixed-phase processes in the simulations, as well as observations from several levels inside convective clouds, would be beneficial to better understand variability of DSD shape in cumulus clouds.

Considering the observed dependence of ϵ on q_c/q_a led to an improvement compared to previous parameterizations that diagnose ϵ from N_c or q_c only, at least for $N_a \leq 900 \text{ cm}^{-3}$. Applying this approach to diagnose μ in bulk microphysics simulations of an isolated cumulus improved offline collision-coalescence rates compared to bulk microphysics simulations that diagnosed μ from N_c. Naturally, for other collision-coalescence parameterizations, the intensity of the sensitivities to μ may differ from that showed here. Further research on the role of μ in other bulk parameterizations of collision-coalescence would be useful. It is also worth noting that the value of μ can impact other microphysical processes, such as sedimentation. The ultimate effect of a given approach on the hydrometeor partitioning and cloud evolution would depend on the balance of all microphysical processes. Additionally, since μ determines the effective radius of cloud droplets, the specific approach chosen impacts the calculation of radiative properties of the clouds, thus having a broader significance for atmospheric models.

The $\epsilon - q_c/q_a$ relationship found in the observations empirically accounts for the effects of the most important broadening mechanisms in cumulus clouds, while the simplicity of its formulation allows application even in single-moment bulk microphysics schemes. However, using q_c/q_a to diagnose ϵ (or μ) in bulk-microphysics models requires accurate representations of intra-cloud variations in q_c, as well as of the cloud base temperature and pressure, thus depending on the model resolution. It should also be considered that deriving μ from DSD measurements over a finite interval of diameters, i.e., based on the incomplete gamma function, as in the observations and bin simulations employed here, could technically be in conflict with the design of bulk microphysics models, which assume that the DSD is described by a *complete* gamma function. Nevertheless, we expect the error introduced by this theoretical discrepancy to be lower than the

uncertainties related to the empirical relationships traditionally used to diagnose μ in bulk microphysics schemes. Although we expect q_c/q_a to be a good proxy for the degree of DSD broadening in general, we emphasize that the specific $\epsilon - q_c/q_a$ relationship illustrated here should not be *a priori* extended to different types of clouds and environmental conditions.

The simulations performed here were not intended to accurately replicate a real cloud, but rather to provide tools that support our interpretation of the observations, in the sense of explaining plausible mechanisms that explain a given behavior of the observable quantities. Analogous experiments, but based on real-case model simulations, would be beneficial.

Data Availability Statement

The TAU microphysics code is hosted by G. Feingold (https://www.esrl.noaa.gov/csd/staff/graham.feingold/code/). The ACRIDICON-CHUVA data employed here is available at http://ftp.cptec.inpe.br/chuva/pesquisa/JGR2021/. The authors employed the WRF model version 3.6.1 (https://doi.org/10.5065/d6mk6b4k).

References

Abade, G. C., Grabowski, W. W., & Pawlowska, H. (2018). Broadening of cloud droplet spectra through eddy hopping: Turbulent entraining parcel simulations. *Journal of the Atmospheric Sciences*, *75*(10), 3365–3379. https://doi.org/10.1175/JAS-D-18-0078.1

Albrecht, B. A. (1989). Aerosols, cloud microphysics, and fractional cloudiness. *Science*, *245*(4923), 1227–1230. https://doi.org/10.1126/science.245.4923.1227

Ayala, O., Rosa, B., & Wang, L.-P. (2008). Effects of turbulence on the geometric collision rate of sedimenting droplets. Part 2. Theory and parameterization. *New Journal of Physics*, *10*(7), 075016. https://doi.org/10.1088/1367-2630/10/7/075016

Ayala, O., Rosa, B., Wang, L.-P., & Grabowski, W. W. (2008). Effects of turbulence on the geometric collision rate of sedimenting droplets. Part 1. Results from direct numerical simulation. *New Journal of Physics*, *10*(7), 075015. https://doi.org/10.1088/1367-2630/10/7/075015

Baker, M. B., Breidenthal, R. E., Choularton, T. W., & Latham, J. (1984). The effects of turbulent mixing in clouds. *Journal of the Atmospheric Sciences*, *41*(2), 299–304. https://doi.org/10.1175/1520-0469(1984)041<0299:teotmi>2.0.co;2

Baker, M. B., Corbin, R. G., & Latham, J. (1980). The influence of entrainment on the evolution of cloud droplet spectra: I. A model of inhomogeneous mixing. *Quarterly Journal of the Royal Meteorological Society*, *106*(449), 581–598. https://doi.org/10.1002/qj.49710644914

Baker, M. B., & Latham, J. (1979). The evolution of droplet spectra and the rate of production of embryonic raindrops in small cumulus clouds. *Journal of the Atmospheric Sciences*, *36*(8), 1612–1615. https://doi.org/10.1175/1520-0469(1979)036<1612:teodsa>2.0.co;2

Baumgardner, D., Brenguier, J., Bucholtz, A., Coe, H., DeMott, P., Garrett, T., et al. (2011). Airborne instruments to measure atmospheric aerosol particles, clouds and radiation: A cook's tour of mature and emerging technology. *Atmospheric Research*, *102*(1), 10–29. https://doi.org/10.1016/j.atmosres.2011.06.021

Baumgardner, D., Jonsson, H., Dawson, W., O'Connor, D., & Newton, R. (2001). The cloud, aerosol and precipitation spectrometer: A new instrument for cloud investigations. *Atmospheric Research*, *59–60*, 251–264. (13th International Conference on Clouds and Precipitation). https://doi.org/10.1016/S0169-8095(01)00119-3

Bera, S., Pandithurai, G., & Prabha, T. V. (2016). Entrainment and droplet spectral characteristics in convective clouds during transition to monsoon. *Atmospheric Science Letters*, *17*(4), 286–293. https://doi.org/10.1002/asl.657

Berry, E. X., & Reinhardt, R. L. (1974). An analysis of cloud drop growth by collection: Part I. Double distributions. *Journal of the Atmospheric Sciences*, *31*(7), 1814–1824. https://doi.org/10.1175/1520-0469(1974)031<1814:aaocdg>2.0.co;2

Blyth, A. M. (1993). Entrainment in cumulus clouds. *Journal of Applied Meteorology*, *32*(4), 626–641. https://doi.org/10.1175/1520-0450(1993)032<0626:eicc>2.0.co;2

Braga, R. C., Rosenfeld, D., Weigel, R., Jurkat, T., Andreae, M. O., Wendisch, M., et al. (2017). Further evidence for CCN aerosol concentrations determining the height of warm rain and ice initiation in convective clouds over the Amazon basin. *Atmospheric Chemistry and Physics*, *17*(23), 14433–14456. https://doi.org/10.5194/acp-17-14433-2017

Brenguier, J.-L., Bachalo, W. D., Chuang, P. Y., Esposito, B. M., Fugal, J., Garrett, T., et al. (2013). In situ measurements of cloud and precipitation particles. In *Airborne measurements for environmental research* (pp. 225–301). https://doi.org/10.1002/9783527653218.ch5

Brenguier, J.-L., & Grabowski, W. W. (1993). Cumulus entrainment and cloud droplet spectra: A numerical model within a two-dimensional dynamical framework. *Journal of the Atmospheric Sciences*, *50*(1), 120–136. https://doi.org/10.1175/1520-0469(1993)050<0120:ceacds>2.0.co;2

Cecchini, M. A., Machado, L. A. T., Andreae, M. O., Martin, S. T., Albrecht, R. I., Artaxo, P., et al. (2017). Sensitivities of Amazonian clouds to aerosols and updraft speed. *Atmospheric Chemistry and Physics*, *17*(16), 10037–10050. https://doi.org/10.5194/acp-17-10037-2017

Cecchini, M. A., Machado, L. A. T., Wendisch, M., Costa, A., Krämer, M., Andreae, M. O., et al. (2017). Illustration of microphysical processes in amazonian deep convective clouds in the gamma phase space: Introduction and potential applications. *Atmospheric Chemistry and Physics*, *17*(23), 14727–14746. https://doi.org/10.5194/acp-17-14727-2017

Chandrakar, K. K., Cantrell, W., Chang, K., Ciochetto, D., Niedermeier, D., Ovchinnikov, M., et al. (2016). Aerosol indirect effect from turbulence-induced broadening of cloud-droplet size distributions. *Proceedings of the National Academy of Sciences*, *113*(50), 14243–14248. https://doi.org/10.1073/pnas.1612686113

Chandrakar, K. K., Cantrell, W., & Shaw, R. A. (2018). Influence of turbulent fluctuations on cloud droplet size dispersion and aerosol indirect effects. *Journal of the Atmospheric Sciences*, *75*(9), 3191–3209. https://doi.org/10.1175/JAS-D-18-0006.1

Chandrakar, K. K., Grabowski, W. W., Morrison, H., & Bryan, G. H. (2021). Impact of entrainment-mixing and turbulent fluctuations on droplet size distributions in a cumulus cloud: An investigation using Lagrangian microphysics with a sub-grid-scale model. *Journal of the Atmospheric Sciences*. https://doi.org/10.1175/JAS-D-20-0281.1

Chen, J., Liu, Y., Zhang, M., & Peng, Y. (2016). New understanding and quantification of the regime dependence of aerosol-cloud interaction for studying aerosol indirect effects. *Geophysical Research Letters*, *43*, 1780–1787. https://doi.org/10.1002/2016GL067683

Chen, J., Liu, Y., Zhang, M., & Peng, Y. (2018). Height dependency of aerosol-cloud interaction regimes. *Journal of Geophysical Research: Atmospheres*, *123*, 491–506. https://doi.org/10.1002/2017JD027431

Chen, S., Yau, M. K., & Bartello, P. (2018). Turbulence effects of collision efficiency and broadening of droplet size distribution in cumulus clouds. *Journal of the Atmospheric Sciences*, *75*(1), 203–217. https://doi.org/10.1175/JAS-D-17-0123.1

Cooper, W. A. (1989). Effects of variable droplet growth histories on droplet size distributions. Part I: Theory. *Journal of the Atmospheric Sciences*, *46*(10), 1301–1311. https://doi.org/10.1175/1520-0469(1989)046<1301:eovdgh>2.0.co;2

Cooper, W. A., Lasher-Trapp, S. G., & Blyth, A. M. (2013). The influence of entrainment and mixing on the initial formation of rain in a warm cumulus cloud. *Journal of the Atmospheric Sciences*, *70*(6), 1727–1743. https://doi.org/10.1175/JAS-D-12-0128.1

Damiani, R., & Vali, G. (2007). Evidence for tilted toroidal circulations in cumulus. *Journal of the Atmospheric Sciences*, *64*(6), 2045–2060. https://doi.org/10.1175/JAS3941.1

Dávila, J., & Hunt, J. C. R. (2001). Settling of small particles near vortices and in turbulence. *Journal of Fluid Mechanics*, *440*, 117–145. https://doi.org/10.1017/S0022112001004694

Devenish, B. J., Bartello, P., Brenguier, J.-L., Collins, L. R., Grabowski, W. W., IJzermans, R. H. A., et al. (2012). Droplet growth in warm turbulent clouds. *Quarterly Journal of the Royal Meteorological Society*, *138*(667), 1401–1429. https://doi.org/10.1002/qj.1897

Dodson, D. S., & Small Griswold, J. D. (2019). Droplet inhomogeneity in shallow cumuli: The effects of in-cloud location and aerosol number concentration. *Atmospheric Chemistry and Physics*, *19*(11), 7297–7317. https://doi.org/10.5194/acp-19-7297-2019

Enukashvily, I. M. (1980). A numerical method for integrating the kinetic equation of coalescence and breakup of cloud droplets. *Journal of the Atmospheric Sciences*, *37*(11), 2521–2534. https://doi.org/10.1175/1520-0469(1980)037<2521:anmfit>2.0.co;2

Feingold, G., Tzivion, S., & Levin, Z. (1988). The evolution of raindrop spectra with altitude 1: Solution to the stochastic collection/breakup equation using the method of moments. *Journal of the Atmospheric Sciences*, *45*, 3387–3399. https://doi.org/10.1175/1520-0469(1988)045<3387:eorspi>2.0.co;2

Ferrier, B. S. (1994). A double-moment multiple-phase four-class bulk ice scheme. Part I: Description. *Journal of the Atmospheric Sciences*, *51*(2), 249–280. https://doi.org/10.1175/1520-0469(1994)051<0249:admmpf>2.0.co;2

Fisch, G., Tota, J., Machado, L. A. T., Silva Dias, M. A. F., Lyra, R. F. d. F., Nobre, C. A., et al. (2004). The convective boundary layer over pasture and forest in Amazonia. *Theoretical and Applied Climatology*, *78*, 47–59. https://doi.org/10.1007/s00704-004-0043-x

Franklin, C. N., Vaillancourt, P. A., Yau, M. K., & Bartello, P. (2005). Collision rates of cloud droplets in turbulent flow. *Journal of the Atmospheric Sciences*, *62*(7), 2451–2466. https://doi.org/10.1175/JAS3493.1

Freud, E., & Rosenfeld, D. (2012). Linear relation between convective cloud drop number concentration and depth for rain initiation. *Journal of Geophysical Research: Atmospheres*, *117*(D2). https://doi.org/10.1029/2011jd016457

Geoffroy, O., Brenguier, J.-L., & Burnet, F. (2010). Parametric representation of the cloud droplet spectra for LES warm bulk microphysical schemes. *Atmospheric Chemistry and Physics*, *10*(10), 4835–4848. https://doi.org/10.5194/acp-10-4835-2010

Grabowski, W. W. (1998). Toward cloud resolving modeling of large-scale tropical circulations: A simple cloud microphysics parameterization. *Journal of the Atmospheric Sciences*, *55*(21), 3283–3298. https://doi.org/10.1175/1520-0469(1998)055<3283:tcrmol>2.0.co;2

Grabowski, W. W., & Abade, G. C. (2017). Broadening of cloud droplet spectra through eddy hopping: Turbulent adiabatic parcel simulations. *Journal of the Atmospheric Sciences*, *74*(5), 1485–1493. https://doi.org/10.1175/JAS-D-17-0043.1

Grabowski, W. W., Dziekan, P., & Pawlowska, H. (2018). Lagrangian condensation microphysics with Twomey CCN activation. *Geoscientific Model Development*, *11*(1), 103–120. https://doi.org/10.5194/gmd-11-103-2018

Grabowski, W. W., & Morrison, H. (2008). Toward the mitigation of spurious cloud-edge supersaturation in cloud models. *Monthly Weather Review*, *136*(3), 1224–1234. https://doi.org/10.1175/2007MWR2283.1

Grabowski, W. W., & Wang, L.-P. (2013). Growth of cloud droplets in a turbulent environment. *Annual Review of Fluid Mechanics*, *45*(1), 293–324. https://doi.org/10.1146/annurev-fluid-011212-140750

Gunthe, S. S., King, S. M., Rose, D., Chen, Q., Roldin, P., Farmer, D. K., et al. (2009). Cloud condensation nuclei in pristine tropical rainforest air of Amazonia: Size-resolved measurements and modeling of atmospheric aerosol composition and CCN activity. *Atmospheric Chemistry and Physics*, *9*(19), 7551–7575. https://doi.org/10.5194/acp-9-7551-2009

Guo, X., Lu, C., Zhao, T., Liu, Y., Zhang, G. J., & Luo, S. (2018). Observational study of the relationship between entrainment rate and relative dispersion in deep convective clouds. *Atmospheric Research*, *199*, 186–192. https://doi.org/10.1016/j.atmosres.2017.09.013

Hartman, C. M., & Harrington, J. Y. (2005). Radiative impacts on the growth of drops within simulated marine stratocumulus. Part I: Maximum solar heating. *Journal of the Atmospheric Sciences*, *62*(7), 2323–2338. https://doi.org/10.1175/JAS3477.1

Hartman, C. M., & Harrington, J. Y. (2005). Radiative impacts on the growth of drops within simulated marine stratocumulus. Part II: Solar zenith angle variations. *Journal of the Atmospheric Sciences*, *62*(7), 2339–2351. https://doi.org/10.1175/JAS3478.1

Hernández Pardo, L., Morrison, H., Machado, L. A. T., Harrington, J. Y., & Lebo, Z. J. (2020). Drop size distribution broadening mechanisms in a bin microphysics Eulerian model. *Journal of the Atmospheric Sciences*, *77*(9), 3249–3273. https://doi.org/10.1175/JAS-D-20-0099.1

Hoffmann, F. (2016). The effect of spurious cloud edge supersaturations in Lagrangian cloud models: An analytical and numerical study. *Monthly Weather Review*, *144*(1), 107–118. https://doi.org/10.1175/MWR-D-15-0234.1

Hoffmann, F., Raasch, S., & Noh, Y. (2015). Entrainment of aerosols and their activation in a shallow cumulus cloud studied with a coupled LCM–LES approach. *Atmospheric Research*, *156*, 43–57. https://doi.org/10.1016/j.atmosres.2014.12.008

Hudson, J. G., & Da, X. (1996). Volatility and size of cloud condensation nuclei. *Journal of Geophysical Research: Atmospheres*, *101*(D2), 4435–4442. https://doi.org/10.1029/95JD00192

Igel, A. L., & van den Heever, S. C. (2017). The role of the gamma function shape parameter in determining differences between condensation rates in bin and bulk microphysics schemes. *Atmospheric Chemistry and Physics*, *17*(7), 4599–4609. https://doi.org/10.5194/acp-17-4599-2017

Jensen, J. B., & Nugent, A. D. (2017). Condensational growth of drops formed on giant sea-salt aerosol particles. *Journal of the Atmospheric Sciences*, *74*(3), 679–697. https://doi.org/10.1175/JAS-D-15-0370.1

Khain, A., Beheng, K. D., Heymsfield, A., Korolev, A., Krichak, S. O., Levin, Z., et al. (2015). Representation of microphysical processes in cloud-resolving models: Spectral (bin) microphysics versus bulk parameterization. *Reviews of Geophysics*, *53*(2), 247–322. https://doi.org/10.1002/2014rg000468

Khain, A., Prabha, T. V., Benmoshe, N., Pandithurai, G., & Ovchinnikov, M. (2013). The mechanism of first raindrops formation in deep convective clouds. *Journal of Geophysical Research: Atmospheres*, *118*(16), 9123–9140. https://doi.org/10.1002/jgrd.50641

Khairoutdinov, M., & Kogan, Y. (2000). A new cloud physics parameterization in a Large-Eddy Simulation model of marine stratocumulus. *Monthly Weather Review*, *128*(1), 229–243. https://doi.org/10.1175/1520-0493(2000)128<0229:ancppi>2.0.co;2

Khvorostyanov, V. I., & Curry, J. A. (1999). Toward the theory of stochastic condensation in clouds. Part II: Analytical solutions of the gamma-distribution type. *Journal of the Atmospheric Sciences*, *56*(23), 3997–4013. https://doi.org/10.1175/1520-0469(1999)056<3997:tttosc>2.0.co;2

Khvorostyanov, V. I., & Curry, J. A. (2008). Analytical solutions to the Stochastic Kinetic Equation for liquid and ice particle size spectra. Part I: Small-size fraction. *Journal of the Atmospheric Sciences*, *65*(7), 2025–2043. https://doi.org/10.1175/2007JAS2484.1

Kogan, Y. (1991). The simulation of a convective cloud in a 3-D model with explicit microphysics. Part I: Model description and sensitivity experiments. *Journal of the Atmospheric Sciences*, *48*(9), 1160–1189. https://doi.org/10.1175/1520-0469(1991)048<1160:tsoacc>2.0.co;2

Kogan, Y. (2013). A cumulus cloud microphysics parameterization for cloud-resolving models. *Journal of the Atmospheric Sciences*, *70*(5), 1423–1436. https://doi.org/10.1175/JAS-D-12-0183.1

Korolev, A. (1995). The influence of supersaturation fluctuations on droplet size spectra formation. *Journal of the Atmospheric Sciences*, *52*(20), 3620–3634. https://doi.org/10.1175/1520-0469(1995)052<3620:tiosfo>2.0.co;2

Korolev, A., Khain, A., Pinsky, M., & French, J. (2016). Theoretical study of mixing in liquid clouds – Part 1: Classical concepts. *Atmospheric Chemistry and Physics*, *16*(14), 9235–9254. https://doi.org/10.5194/acp-16-9235-2016

Kumar, B., Götzfried, P., Suresh, N., Schumacher, J., & Shaw, R. A. (2018). Scale dependence of cloud microphysical response to turbulent entrainment and mixing. *Journal of Advances in Modeling Earth Systems*, *10*(11), 2777–2785. https://doi.org/10.1029/2018MS001487

Lance, S. (2012). Coincidence errors in a Cloud Droplet Probe (CDP) and a Cloud and Aerosol Spectrometer (CAS), and the improved performance of a modified CDP. *Journal of Atmospheric and Oceanic Technology*, *29*(10), 1532–1541. https://doi.org/10.1175/JTECH-D-11-00208.1

Lance, S., Brock, C. A., Rogers, D., & Gordon, J. A. (2010). Water droplet calibration of the Cloud Droplet Probe (CDP) and in-flight performance in liquid, ice and mixed-phase clouds during ARCPAC. *Atmospheric Measurement Techniques*, *3*(6), 1683–1706. https://doi.org/10.5194/amt-3-1683-2010

Lasher-Trapp, S. G., Cooper, W. A., & Blyth, A. M. (2005). Broadening of droplet size distributions from entrainment and mixing in a cumulus cloud. *Quarterly Journal of the Royal Meteorological Society*, *131*(605), 195–220. https://doi.org/10.1256/qj.03.199

Latham, J., & Reed, R. L. (1977). Laboratory studies of the effects of mixing on the evolution of cloud droplet spectra. *Quarterly Journal of the Royal Meteorological Society*, *103*(436), 297–306. https://doi.org/10.1002/qj.49710343607

Lebo, Z. J., Johnson, N. C., & Harrington, J. Y. (2008). Radiative influences on ice crystal and droplet growth within mixed-phase stratus clouds. *Journal of Geophysical Research: Atmospheres*, *113*(D9). https://doi.org/10.1029/2007JD009262

Lin, Y.-L., Farley, R. D., & Orville, H. D. (1983). Bulk parameterization of the snow field in a cloud model. *Journal of Climate and Applied Meteorology*, *22*(6), 1065–1092. https://doi.org/10.1175/1520-0450(1983)022<1065:bpotsf>2.0.co;2

Liu, Y., & Daum, P. H. (2002). Indirect warming effect from dispersion forcing. *Nature*, *419*, 580–581. https://doi.org/10.1038/419580a

Liu, Y., Daum, P. H., Guo, H., & Peng, Y. (2008). Dispersion bias, dispersion effect, and the aerosol–cloud conundrum. *Environmental Research Letters*, *3*(4), 045021. https://doi.org/10.1088/1748-9326/3/4/045021

Liu, Y., Daum, P. H., & Yum, S. S. (2006). Analytical expression for the relative dispersion of the cloud droplet size distribution. *Geophysical Research Letters*, *33*. https://doi.org/10.1029/2005GL024052

Lu, C., Liu, Y., Yum, S. S., Chen, J., Zhu, L., Gao, S., et al. (2020). Reconciling contrasting relationships between relative dispersion and volume-mean radius of cloud droplet size distributions. *Journal of Geophysical Research: Atmospheres*, *125*, e2019JD031868. https://doi.org/10.1029/2019JD031868

Lu, C., Niu, S., Liu, Y., & Vogelmann, A. M. (2013). Empirical relationship between entrainment rate and microphysics in cumulus clouds. *Geophysical Research Letters*, *40*, 2333–2338. https://doi.org/10.1002/grl.50445

Lu, J., Nordsiek, H., & Shaw, R. A. (2010). Clustering of settling charged particles in turbulence: Theory and experiments. *New Journal of Physics*, *12*(12), 123030. https://doi.org/10.1088/1367-2630/12/12/123030

Lu, M.-L., Conant, W. C., Jonsson, H. H., Varutbangkul, V., Flagan, R. C., & Seinfeld, J. H. (2007). The marine stratus/stratocumulus experiment (MASE): Aerosol-cloud relationships in marine stratocumulus. *Journal of Geophysical Research: Atmospheres*, *112*(D10). https://doi.org/10.1029/2006JD007985

Luo, S., Lu, C., Liu, Y., Bian, J., Gao, W., Li, J., et al. (2020). Parameterizations of entrainment-mixing mechanisms and their effects on cloud droplet spectral width based on numerical simulations. *Journal of Geophysical Research: Atmospheres*, *125*, e2020JD032972. https://doi.org/10.1029/2020JD032972

MacCready, P. B., & Takeuchi, D. M. (1968). Precipitation initiation mechanisms and droplet characteristics of some convective cloud cores. *Journal of Applied Meteorology and Climatology*, *7*(4), 591–602. https://doi.org/10.1175/1520-0450(1968)007<0591:pimadc>2.0.co;2

Machado, L. A. T., Dias, M. A. F. S., Morales, C., Fisch, G., Vila, D., Albrecht, R., et al. (2014). The CHUVA Project: How does convection vary across Brazil? *Bulletin of the American Meteorological Society*, *95*(9), 1365–1380. https://doi.org/10.1175/bams-d-13-00084.1

Mallaun, C., Giez, A., & Baumann, R. (2015). Calibration of 3-D wind measurements on a single-engine research aircraft. *Atmospheric Measurement Techniques*, *8*(8), 3177–3196. https://doi.org/10.5194/amt-8-3177-2015

Martin, G., Johnson, D., & Spice, A. (1994). The measurement and parameterization of effective radius of droplets in warm stratocumulus clouds. *Journal of the Atmospheric Sciences*, *51*(13), 1823–1842. https://doi.org/10.1175/1520-0469(1994)051<1823:tmapoe>2.0.co;2

Martin, S. T., Andreae, M. O., Artaxo, P., Baumgardner, D., Chen, Q., Goldstein, A. H., & Trebs, I. (2010). Sources and properties of Amazonian aerosol particles. *Reviews of Geophysics*, *6*(2). https://doi.org/10.1029/2008rg000280

Miles, N. L., Verlinde, J., & Clothiaux, E. E. (2000). Cloud droplet size distributions in low-level stratiform clouds. *Journal of the Atmospheric Sciences*, *57*(2), 295–311. https://doi.org/10.1175/1520-0469(2000)057<0295:cdsdil>2.0.co;2

Molleker, S., Borrmann, S., Schlager, H., Luo, B., Frey, W., Klingebiel, M., et al. (2014). Microphysical properties of synoptic-scale polar stratospheric clouds: In situ measurements of unexpectedly large HNO-containing particles in the Arctic vortex. *Atmospheric Chemistry and Physics*, *14*(19), 10785–10801. https://doi.org/10.5194/acp-14-10785-2014

Morrison, H., & Grabowski, W. W. (2007). Comparison of bulk and bin warm-rain microphysics models using a kinematic framework. *Journal of the Atmospheric Sciences*, *64*(8), 2839–2861. https://doi.org/10.1175/jas3980

Morrison, H., & Grabowski, W. W. (2008). Modeling supersaturation and subgrid-scale mixing with two-moment bulk warm microphysics. *Journal of the Atmospheric Sciences*, *65*(3), 792–812. https://doi.org/10.1175/2007JAS2374.1

Morrison, H., Thompson, G., & Tatarskii, V. (2009). Impact of cloud microphysics on the development of trailing stratiform precipitation in a simulated squall line: Comparison of one-and two-moment schemes. *Monthly Weather Review*, *137*(3), 991–1007. https://doi.org/10.1175/2008mwr2556.1

Morrison, H., van, Lier-Walqui, M., Fridlind, A. M., Grabowski, W. W., Harrington, J. Y., Hoose, C., et al. (2020). Confronting the challenge of modeling cloud and precipitation microphysics. *Journal of Advances in Modeling Earth Systems*, *12*(8), e2019MS001689. https://doi.org/10.1029/2019MS001689

Morrison, H., Witte, M., Bryan, G. H., Harrington, J. Y., & Lebo, Z. J. (2018). Broadening of modeled cloud droplet spectra using bin microphysics in an Eulerian spatial domain. *Journal of the Atmospheric Sciences*, *75*(11), 4005–4030. https://doi.org/10.1175/JAS-D-18-0055.1

NCAR. (2018). *The NCAR Command Language* (Version 6.5.0). Boulder, Colorado: UCAR/NCAR/CISL/TDD. https://doi.org/10.5065/D6WD3XH5

Ovtchinnikov, M., & Easter, R. C. (2009). Nonlinear advection algorithms applied to interrelated tracers: Errors and implications for modeling aerosol–cloud interactions. *Monthly Weather Review*, *137*(2), 632–644. https://doi.org/10.1175/2008MWR2626.1

Pawlowska, H., Grabowski, W. W., & Brenguier, J.-L. (2006). Observations of the width of cloud droplet spectra in stratocumulus. *Geophysical Research Letters*, *33*. https://doi.org/10.1029/2006GL026841

Peng, Y., & Lohmann, U. (2003). Sensitivity study of the spectral dispersion of the cloud droplet size distribution on the indirect aerosol effect. *Geophysical Research Letters*, *30*(10). https://doi.org/10.1029/2003GL017192

Petters, M. D., & Kreidenweis, S. M. (2007). A single parameter representation of hygroscopic growth and cloud condensation nucleus activity. *Atmospheric Chemistry and Physics*, *7*(8), 1961–1971. https://doi.org/10.5194/acp-7-1961-2007

Pinsky, M., & Khain, A. (2018). Theoretical analysis of mixing in liquid clouds – Part IV: DSD evolution and mixing diagrams. *Atmospheric Chemistry and Physics*, *18*(5), 3659–3676. https://doi.org/10.5194/acp-18-3659-2018

Pinsky, M., Khain, A., & Korolev, A. (2016). Theoretical analysis of mixing in liquid clouds – Part 3: Inhomogeneous mixing. *Atmospheric Chemistry and Physics*, *16*(14), 9273–9297. https://doi.org/10.5194/acp-16-9273-2016

Pinsky, M., Khain, A., Korolev, A., & Magaritz-Ronen, L. (2016). Theoretical investigation of mixing in warm clouds – Part 2: Homogeneous mixing. *Atmospheric Chemistry and Physics*, *16*(14), 9255–9272. https://doi.org/10.5194/acp-16-9255-2016

Pinsky, M., & Khain, A. P. (2002). Effects of in-cloud nucleation and turbulence on droplet spectrum formation in cumulus clouds. *Quarterly Journal of the Royal Meteorological Society*, *128*(580), 501–533. https://doi.org/10.1256/003590002321042072

Pinsky, M., Khain, A. P., Grits, B., & Shapiro, M. (2006). Collisions of small drops in a turbulent flow. Part III: Relative droplet fluxes and swept volumes. *Journal of the Atmospheric Sciences*, *63*(8), 2123–2139. https://doi.org/10.1175/JAS3730.1

Pinsky, M., Khain, A. P., & Shapiro, M. (2007). Collisions of cloud droplets in a turbulent flow. Part IV: Droplet hydrodynamic interaction. *Journal of the Atmospheric Sciences*, *64*(7), 2462–2482. https://doi.org/10.1175/JAS3952.1

Pöhlker, M. L., Ditas, F., Saturno, J., Klimach, T., Hrabě de Angelis, I., Araùjo, A. C., et al. (2018). Long-term observations of cloud condensation nuclei over the Amazon rain forest – Part 2: Variability and characteristics of biomass burning, long-range transport, and pristine rain forest aerosols. *Atmospheric Chemistry and Physics*, *18*(14), 10289–10331. https://doi.org/10.5194/acp-18-10289-2018

Pöhlker, M. L., Pöhlker, C., Ditas, F., Klimach, T., Hrabe de Angelis, I., Araújo, A., et al. (2016). Long-term observations of cloud condensation nuclei in the Amazon rain forest – Part 1: Aerosol size distribution, hygroscopicity, and new model parametrizations for CCN prediction. *Atmospheric Chemistry and Physics*, *16*(24), 15709–15740. https://doi.org/10.5194/acp-16-15709-2016

Reutter, P., Su, H., Trentmann, J., Simmel, M., Rose, D., Gunthe, S. S., et al. (2009). Aerosol- and updraft-limited regimes of cloud droplet formation: Influence of particle number, size and hygroscopicity on the activation of cloud condensation nuclei (CCN). *Atmospheric Chemistry and Physics*, *9*(18), 7067–7080. https://doi.org/10.5194/acp-9-7067-2009

Rogers, D. P., Telford, J. W., & Chai, S. K. (1985). Entrainment and the temporal development of the microphysies of convective clouds. *Journal of Atmospheric Sciences*, *42*(17), 1846–1858. https://doi.org/10.1175/1520-0469(1985)042<1846:eattdo>2.0.co;2

Rotstayn, L. D., & Liu, Y. (2003). Sensitivity of the first indirect aerosol effect to an increase of cloud droplet spectral dispersion with droplet number concentration. *Journal of Climate*, *16*(21), 3476–3481. https://doi.org/10.1175/1520-0442(2003)016<3476:sotfia>2.0.co;2

Seifert, A., & Beheng, K. D. (2006). A two-moment cloud microphysics parameterization for mixed-phase clouds. Part 1: Model description. *Meteorology and Atmospheric Physics*, *92*, 45–66. https://doi.org/10.1007/s00703-005-0112-4

Seifert, A., Leinonen, J., Siewert, C., & Kneifel, S. (2019). The geometry of rimed aggregate snowflakes: A modeling study. *Journal of Advances in Modeling Earth Systems*, *11*(3), 712–731. https://doi.org/10.1029/2018MS001519

Shima, S., Kusano, K., Kawano, A., Sugiyama, T., & Kawahara, S. (2009). The super-droplet method for the numerical simulation of clouds and precipitation: A particle-based and probabilistic microphysics model coupled with a non-hydrostatic model. *Quarterly Journal of the Royal Meteorological Society*, *135*(642), 1307–1320. https://doi.org/10.1002/qj.441

Skamarock, W. C., Klemp, J. B., Dudhia, J., Gill, D. O., Barker, D. M., Duda, M. G., & Powers, J. G. (2008). In *A description of the Advanced Research WRF version 3 (No. NCAR/TN-475+STR)*. University Corporation for Atmospheric Research. https://doi.org/10.5065/D68S4MVH

Spanu, A., Dollner, M., Gasteiger, J., Bui, T. P., & Weinzierl, B. (2020). Flow-induced errors in airborne in situ measurements of aerosols and clouds. *Atmospheric Measurement Techniques*, *13*(4), 1963–1987. https://doi.org/10.5194/amt-13-1963-2020

Squires, P. (1958). The microstructure and colloidal stability of warm clouds. Part I — The relation between structure and stability. *Tellus*, *10*(2), 256–261. https://doi.org/10.1111/j.2153-3490.1958.tb02011.x

Squires, P. (1958). The microstructure and colloidal stability of warm clouds. Part II — The causes of the variations in microstructure. *Tellus*, *10*(2), 262–271. https://doi.org/10.1111/j.2153-3490.1958.tb02012.x

Stevens, B., Feingold, G., Cotton, W. R., & Walko, R. L. (1996). Elements of the microphysical structure of numerically simulated nonprecipitating stratocumulus. *Journal of the Atmospheric Sciences*, *53*(7), 980–1006. https://doi.org/10.1175/1520-0469(1996)053<0980:eotmso>2.0.co;2

Stevens, B., Walko, R. L., Cotton, W. R., & Feingold, G. (1996). The spurious production of cloud-edge supersaturations by Eulerian models. *Monthly Weather Review*, *124*(5), 1034–1041. https://doi.org/10.1175/1520-0493(1996)124<1034:tspoce>2.0.co;2

Tölle, M. H., & Krueger, S. K. (2014). Effects of entrainment and mixing on droplet size distributions in warm cumulus clouds. *Journal of Advances in Modeling Earth Systems*, *6*(2), 281–299. https://doi.org/10.1002/2012MS000209

Thompson, G., Field, P. R., Rasmussen, R. M., & Hall, W. D. (2008). Explicit forecasts of winter precipitation using an improved bulk microphysics scheme. Part II: Implementation of a new snow parameterization. *Monthly Weather Review*, *136*, 5095–5115. https://doi.org/10.1175/2008mwr2387.1

Tzivion, S., Feingold, G., & Levin, Z. (1987). An efficient numerical solution to the stochastic collection equation. *Journal of the Atmospheric Sciences*, *44*(21), 3139–3149. https://doi.org/10.1175/1520-0469(1987)044<3139:aenstt>2.0.co;2

Tzivion, S., Feingold, G., & Levin, Z. (1989). The evolution of raindrop spectra. Part II: Collisional collection/breakup and evaporation in a rainshaft. *Journal of the Atmospheric Sciences*, *46*(21), 3312–3328. https://doi.org/10.1175/1520-0469(1989)046<3312:teorsp>2.0.co;2

Vaillancourt, P. A., Yau, M. K., & Grabowski, W. W. (1997). Upshear and downshear evolution of cloud structure and spectral properties. *Journal of the Atmospheric Sciences*, *54*(9), 1203–1217. https://doi.org/10.1175/1520-0469(1997)054<1203:uadeoc>2.0.co;2

Wang, L.-P., Ayala, O., Rosa, B., & Grabowski, W. W. (2008). Turbulent collision efficiency of heavy particles relevant to cloud droplets. *New Journal of Physics*, *10*(7), 075013. https://doi.org/10.1088/1367-2630/10/7/075013

Wang, Y., & Geerts, B. (2013). Composite vertical structure of vertical velocity in nonprecipitating cumulus clouds. *Monthly Weather Review*, *141*(5), 1673–1692. https://doi.org/10.1175/MWR-D-12-00047.1

Wang, Y., Zhao, C., McFarquhar, G. M., Wu, W., Reeves, M., & Li, J. (2021). Dispersion of droplet size distributions in supercooled non-precipitating stratocumulus from aircraft observations obtained during the Southern Ocean Cloud Radiation Aerosol Transport Experimental Study. *Journal of Geophysical Research: Atmospheres*, *126*, e2020JD033720. https://doi.org/10.1029/2020JD033720

Weigel, R., Spichtinger, P., Mahnke, C., Klingebiel, M., Afchine, A., Petzold, A., et al. (2016). Thermodynamic correction of particle concentrations measured by underwing probes on fast-flying aircraft. *Atmospheric Measurement Techniques*, *9*(10), 5135–5162. https://doi.org/10.5194/amt-9-5135-2016

Wendisch, M., Pöschl, U., Andreae, M. O., Machado, L. A. T., Albrecht, R., Schlager, H., et al. (2016). The ACRIDICON-CHUVA campaign: Studying tropical deep convective clouds and precipitation over Amazonia using the new German research aircraft HALO. *Bulletin of the American Meteorological Society*, *97*(10), 1885–1908. https://doi.org/10.1175/BAMS-D-14-00255.1

Yang, F., Kollias, P., Shaw, R. A., & Vogelmann, A. M. (2018). Cloud droplet size distribution broadening during diffusional growth: Ripening amplified by deactivation and reactivation. *Atmospheric Chemistry and Physics*, *18*(10), 7313–7328. https://doi.org/10.5194/acp-18-7313-2018

Yeom, J. M., Yum, S. S., Mei, F., Schmid, B., Comstock, J., Machado, L. A., & Cecchini, M. A. (2019). Impact of secondary droplet activation on the contrasting cloud microphysical relationships during the wet and dry seasons in the Amazon. *Atmospheric Research*, *230*, 104648. https://doi.org/10.1016/j.atmosres.2019.104648

Yin, Y., Levin, Z., Reisin, T. G., & Tzivion, S. (2000). The effects of giant cloud condensation nuclei on the development of precipitation in convective clouds—A numerical study. *Atmospheric Research*, *53*(1), 91–116. https://doi.org/10.1016/s0169-8095(99)00046-0

Zhao, M., & Austin, P. H. (2005). Life cycle of numerically simulated shallow cumulus clouds. Part II: Mixing dynamics. *Journal of the Atmospheric Sciences*, *62*(5), 1291–1310. https://doi.org/10.1175/JAS3415.1